Electrical measurements of femtosecond laser treated graphene

Master's Thesis, 11.05.2017

Author:

Jyrki Manninen

Supervisor:

Andreas Johansson

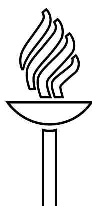

UNIVERSITY OF JYVÄSKYLÄ
DEPARTMENT OF PHYSICS

Abstract

Jyrki Manninen
Electrical measurements of femtosecond laser treated graphene
Master's thesis
Department of Physics, University of Jyväskylä, 63 pages

The main goal of this thesis was to fabricate graphene devices suitable for electrical measurements and research femtosecond laser induced functionalization of the devices. The research required synthesis of graphene by chemical vapor deposition at high temperature and fabrication of device geometry and electrical measurements of pristine and laser treated graphene. The synthesis was done on catalytic copper thin films from liquid ethanol added by bubbling and gaseous methane as carbon sources and it was found that the gaseous methane provides more repeatable concentration of carbon during the synthesis. It was also found that the steel based loading system caused damage to the catalytic surface and a quartz based system resulted in more consistent growth platform for the graphene. The post-synthesis processing of the graphene was done by a process with metal thin films between patterning resits and graphene to avoid adding resists residues on the graphene. The method developed in the thesis was able to provide a reliable method to produce measurable graphene devices. The electrical measurements of the graphene were done for pristine samples in ambient atmosphere, N_2, different humidities and lower temperatures. The gated measurements provided information about the density of states limited conductance and charging effects on the graphene by atmospheric molecules and charge traps. The femtosecond functionalization of graphene was done in N_2 and ambient atmosphere. In ambient atmosphere the treatment resulted in oxidized graphene and it was possible to induce the oxidization gradually by repeated treatment steps towards a fully insulating state whilst preserving the structural continuity of the graphene device. The oxidization is only done to features in contact with the ambient atmosphere and it was found out that for example folds can be used to mask graphene from the oxidization. In N_2 atmosphere the treatment resulted in n-type doping, amount of which depends on the power of the treatment. The n-type doping resulted in a high counter charging or screening in ambient atmosphere and also was slowly countered by charge traps in the substrate. The n-type doping by femtosecond laser was also used to pattern an unevenly doped diffusive graphene channel. Femtosecond laser induced treatment offers multiple ways to engineer graphene based electronics.

Keywords: Graphene, graphene oxide, electrical properties, femtosecond laser, doping, functionalization

Tiivistelmä

Jyrki Manninen
Sähköisiä mittauksia femtosekuntilaserilla käsitelylle grafeenille
Pro Gradu -tutkielma
Fysiikan laitos, Jyväskylän yliopisto, 2017, 63 sivua

Tutkielman pääasiallinen tavoite oli valmistaa sähköisiin mittauksiin sopivia grafeenilaitteita ja tutkia femtosekuntilaserkäsittelyn vaikutusta grafeenin sähköisiin ominaisuuksiin. Tutkielmassa käsitellään grafeenin valmistamista kemiallisella kaasufaasipinnoituksella, laitegeometrian määrittelyä ja käsittelemättömän, sekä femtosekuntilaserilla käsitellyn grafeenin sähköisiä mittauksia. Grafeenin synteesin alustana käytettiin kupariohutkalvoja ja pääasiallisena lähtöaineena oli etanoli tai metaani. Metaanin käyttö grafeenin synteesissä johti paremmin toistettaviin tuloksiin. Lisäksi havaittiin, että synteesissä käytetyn uunin latausjärjestelmän teräksinen osa lisäsi kupariohutkalvon reikiintymistä synteesin aikana. Teräsosan vaihtaminen kvartsiin vähensi huomattavasti reikiintymistä. Laitegeometria määriteltiin käyttämällä elektronimikroskooppi pohjaista litografiaa. Prosessissa grafeenin ja resistin väliin höyrystettiin ohut metallikalvo, jonka avulla pyrittiin välttämään resististä jääviä epäpuhtauksia grafeenilaitteiden pinnalla. Grafeenin sähköisiä ominaisuuksia mitattiin huoneilmassa, typessä, kosteuskammiossa ja matalassa lämpötilassa. Mittauksista pystyi näkemään grafeenin varauksenkuljettajatiheyden määrittämän sähkönjohtavuuden, sekä ilmakehän hiukkasten ja substraatin varausansojen varauksen vaikutuksen varauksenkuljettajatiheyteen. Grafeenin femtosekuntilaserkäsittely tehtiin typessä ja huoneilmassa. Huoneilmassa tehty käsittely hapetti grafeenin nostaen samalla sen sähköistä vastusta. Hapetuksen vahvuutta pystyttiin lisäämään askeleittain tai vaihtoehtoisesti grafeenin voitiin hapettaa suoraan eristäviä kuvioita. Käsittely hapetti grafeenin rikkomatta hilan yhtenäisyyttä ja reaktio näytti tapahtuvan vain päällimmäisille, ilmakehän kanssa kosketuksissa oleville, kerroksille. Typessä tehty femtosekuntilaserkäsittely lisäsi negatiivisten varauksenkuljettajien määrää grafeenissa (n-tyyppinen douppaus) ja tämän käsittelyn avulla pystyttiin määrittämään myös epätasaisia varauksenkuljettajaprofiileja grafeeniin. Typessä käsitelty grafeeni vuorovaikutti huomattavasti huoneilman molekyylien ja substraattien varausansojen kanssa.

Avainsanat: Grafeeni, grafeenioksidi, sähköiset ominaisuudet, femtosekuntilaser, douppaus, funktionalisaatio

Acknowledgements

The experiments in this thesis would not have been possible without the help of many skilled people working and/or studying at University of Jyväskylä and the contribution of the people mentioned here has been crucial to completion of the thesis. Among these contributors I have also received miscellaneous assistance in many cases from the people working at Nanoscience Center which has been greatly appreciated and I hope that the helpful and friendly atmosphere present at NSC is never lost.

First I would like to thank and acknowledge my instructor Andreas Johansson for his assistance in the experiments and also the deep interest he showed for the research. Vesa-Matti Hiltunen and Kevin Roberts were also crucial especially in the beginning of the work as they introduced me to many of the methods I have used during the thesis and they are thanked for their assistance in synthesis, fabrication and characterization of the samples and for multiple discussion on ideas. The femtosecond-laser based imaging and patterning would not have been possible without the patient help of Jukka Aumanen who handled the lasers during the experiments and his contribution to the experiments is greatly appreciated. In the field of laser I also acknowledge and thank for the assistance of Pasi Myllyperkiö and Juha Koivistoinen who helped me in the measurements done during the thesis. The assistance in the handling of laboratory equipment and work used to keep them running by laboratory engineers Kimmo Kinnunen and Tarmo Suppula is also greatly valued. Kirsi Mäki is thanked for help with vector graphics. Lastly I would like to thank my parents Ilkka and Taina Manninen for my upbringing and financial support during my studies.

Contents

Abstract **3**

Tiivistelmä **4**

Acknowledgements **5**

1 Introduction **7**

2 Theoretical background **9**

2.1 The band-structure of graphene and linear low-energy dispersion 9

2.2 Conductivity of a graphene junction from idealized model 12

2.3 Graphene in a measurement setup 15

3 Experimental methods **20**

3.1 Sample fabrication: Chemical vapour deposition, transfer and device fabrication 20

3.2 Materials and methods: graphene synthesis and device fabrication 23

3.3 Materials and methods for electrical measurements for pristine and femtosecond laser treated graphene 27

4 Experimental results **29**

4.1 The results of synthesis and device fabrication 29

4.2 Resistance of graphene devices with two-probe and four-probe measurements. 35

4.3 Back-gated measurements of pristine graphene 39

4.4 Oxidization of graphene by laser in ambient air 43

4.5 Doping of graphene by femtosecond laser in N_2 50

5 Conclusions **56**

Appendices **63**

1 Introduction

The ever increasing complexity and demand for advanced technology requires manipulation of matter at the nanoscale or even at the atomic level. Nanomaterials are an example of such technology with structure defined by nanometer-scale building blocks. The properties of these materials can be engineered in more precise manner to have the best possible combination of features for the chosen application. The field of nanomaterials has the interdisciplinarity of sciences built in as these materials are researched in molecular biology, chemistry, nanophysics and even medical science. Nanomaterials come in many shapes derived from cells or synthetized in laboratories.

One group of nanomaterials researched widely in recent years are the ultra thin two-dimensional materials which can be only a single layer of atoms thick. The two-dimensional materials were considered more a theoretical form of matter rather than a real material until the experimental realization of graphene, a hexagonally aligned layer of carbon atoms, by A. Geim and K. S. Novoselov at 2004 (Nobel Prize 2010) [1]. After the discovery of graphene, the two-dimensional group of materials has been expanded by a variety of different materials such as hexagonal boron nitride ($h-\mathrm{BN}$) and transition metal dichalcogenides ($\mathrm{MoS_2}, \mathrm{NbSe_2}$...) [2]. The number of possible two-dimensional systems grows even larger when one takes into account the possible heterostructures build by combining individual layers of these materials [3].

Despite emergency of new 2D-materials graphene is still being widely researched as it has been shown that the hexagonally aligned web of carbon atoms might pack a punch when it comes to future of nanotechnology. The mechanical strength of graphene is unmatched and so is the mobility of the charge carriers [4, 5]. The electric current in graphene is transmitted by massless Dirac fermions, which gives rise to exotic transport properties such as the quantum hall effect, chiral tunneling and electron optics [6–8]. Even stress in graphene can be exciting as it creates pseudomagnetism, strength of which can be comparable to a magnetic field of 300 T [9]. However despite the exotic and superior properties, the application of graphene to products may prove difficult due to challenges in production of large-scale continuous homogeneous graphene lattices. However even non-perfect graphene lattices can prove valuable in science and for example the fact that graphene has no bulk, just surface, can be a powerful tool for example in gas sensing [10,11].

In its natural form graphene is found as a part of its bulk material, graphite, which is formed by randomly stacked graphene sheets. The bonding of these sheets to each other is mediated by weaker van der Waals forces, but the in-plane structure of the sheets is bound by strong covalent bonding. The weak bonding between planes means that the fabrication of graphene can be achieved by starting with graphite and mechanically or chemically exfoliating the layers but it has proven difficult to produce large uniform films of graphene with a top down approach [1, 12]. The bottom-up fabrication of graphene starts with a source of carbon for example a molecule, which is broken down to atomic carbon which form graphene. This can be achieved by means of chemical vapour deposition, a method which has promise in producing large continuous graphene films [13, 14]. A problem often encountered with CVD is that the graphene films produced composed of multiple grains grown together to form a single continuous layer, which often breaks the hexagonal structure of the lattice causing increased scattering [15]. Electronic devices of graphene require additional processing steps for the graphene such as trasfer, fabrication

of electrodes and etching of the graphene to wanted device geometry. These steps often require supporting and masking graphene with resists which can result in a lowered electronic quality.

Further functionalization of graphene has been recently done by two-photon induced oxidation at University of Jyväskylä [16]. In this work Aumanen et al. used femtosecond pulsed laser to draw oxidization patterns on graphene which resulted in insulating device. The goal of this study was to further investigate the effects of femtosecond-laser treatment in N_2 and in air on the properties of graphene devices. The work towards this goal included improvements towards the CVD production of graphene at University of Jyväskylä, fabrication of graphene devices suitable for the measurements by avoiding additional resist/graphene contact and electrical charasteristication of the devices before the treatment in different atmospheres. The results of this thesis reassure that the two-photon oxidization turns graphene gradually insulating locally and additionally shows that only the top layer is oxidized and the lower levels of multilayered structures stay conductive. The treatment in N_2 resulted in n-type doping of the graphene devices.

2 Theoretical background

2.1 The band-structure of graphene and linear low-energy dispersion

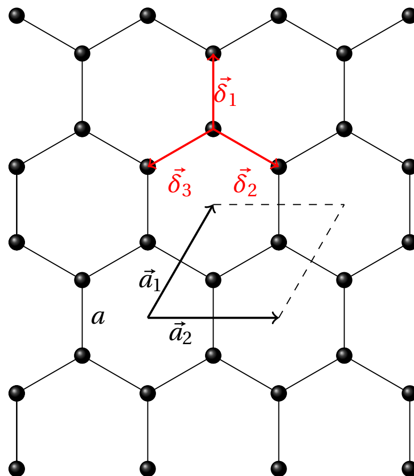

Figure 1. The hexagonal honeycomb structure of graphene formed by sp^2 hybridized carbon atoms. The bond length a is 1.42 Å. The unit cell of graphene is defined by the vectors $\vec{a_1}$ and $\vec{a_2}$ and the $\vec{\delta_1}$, $\vec{\delta_2}$ and $\vec{\delta_3}$ define the nearest neighbours used in the tight-binding approximation.

The electronic properties of solid state matter in a periodic lattice are often described by using the band theory. The band theory is used to derive the states of electrons in continuous lattices as energy bands and especially the energy bands in the vicinity of the ground state are used to model the behaviour of the electrons in materials. In insulators the energy bands up to Fermi energy are filled and the next band (conduction band) is separated by a high energy difference (band gap) from the highest occupied band (valence band). The electrons can't propagate in bands with filled states and the band gap means that they require the energy of gap or more be excited from valence band to the conduction band. In semiconductors the gap is smaller and at finite temperatures a statistically significant portion of the electrons are excited to the conduction band. Both the excited electrons and the vacant states in the valence band can act as charge carriers. In metals there is no energy gap between the bands can overlap partially which means that metallic material is conductive even at the ground state. Graphene as a material is often described as semimetal or zero gap semiconductor as the band structure is slightly different from the materials described earlier: the valence and conduction bands do not overlap but there is no band gap.

The band structure of graphene results from the honeycomb symmetry of the lattice seen in figure 1 and the sp^2 hybridized carbon atoms of the lattice. The sp^2 hybridized carbon atoms form 3 σ -bonds with their neighbouring atoms with length of 1.42 Å and one electron is delocalized in the π-bonding orbitals of lattice. The energies of σ-bonding electrons are far away from the ground state compared to the π-bonding electrons and the σ-bonding electrons are not taken into account when calculating the energy bands. In addition the π electrons are only allowed nearest neighbour hopping and the other transitions are disregarded. These approximations along with the tight-binding approximation can be

used to derive the dispersion relation [17, 18]:

$$E(q_x, q_y) = \pm t\sqrt{3 + 2\cos(\sqrt{3}q_y a) + 4\cos(\frac{\sqrt{3}q_y a}{2})\cos(\frac{3q_x a}{2})}. \tag{1}$$

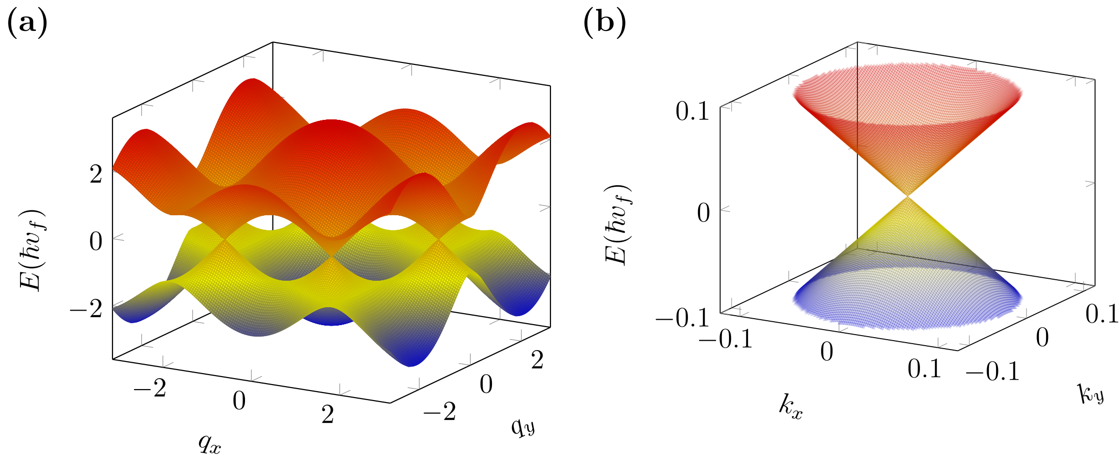

Figure 2. The dispersion relation of graphene and the first order approximation in the vicinity of Fermi energy. The conduction band is the upper red surface and the valence band is the yellow-blue surface. **(a)** The energy dispersion of equation (1) of graphene obtained from the tight-binding approximation. **(b)** The first order approximation of the dispersion relation (eq. (4)) plotted in the vicinity of a Dirac point.

In equation (1), t corresponds to the hopping energy, a is the length of the carbon-carbon bond in the graphene lattice and q_x and q_y are the momentum vectors of electrons in the two-dimensional material. The dispersion relation is plotted in 2a. As seen in the plot there are a few points at the fermi energy ($E = 0$) where conduction band and valence band meets. There are six of these points at each corner of the first Brillouin zone. These points can be described by two linearly independent $\vec{q}$ vectors that result in $E(\vec{q}) = 0$:

$$\vec{K} = \left(\frac{2\pi}{3a}, \frac{2\pi}{3\sqrt{3}a}\right) \text{ and } \vec{K'} = \left(\frac{2\pi}{3a}, -\frac{2\pi}{3\sqrt{3}a}\right). \tag{2}$$

The energy in the vicinity of these points ($\vec{K}$ or $\vec{K'}$ in (2)) can be approximated by expanding it with respect to these Dirac valleys around the Dirac points, $\vec{K}$ and $\vec{K'}$, by noting $\vec{q} + \vec{K}$ as $\vec{k}$ or $\vec{q} + \vec{K'}$ as $\vec{k}$. The resulting simplified tight-binding hamiltonian can be written as [17]:

$$H_g \approx \hbar v_F \begin{bmatrix} 0 & k_x \mp ik_y \\ k_x \pm ik_y & 0 \end{bmatrix} \tag{3}$$

The hamiltonian of (3) includes both of the Dirac valleys by the upper and lower signs. The eigenvalues of both valleys are the same, resulting in a two times degenerate dispersion relation which reads as:

$$E(k_x, k_y) = \pm\hbar v_F\sqrt{k_x^2 + k_y^2} = \pm\hbar v_F|\vec{k}|. \tag{4}$$

In equation (4) $\vec{k} = \vec{k_x} + \vec{k_y}$ is an arbitrary momentum vector with respect to $\vec{K}$ or $\vec{K'}$. The relation is only dependent on the length of $\vec{k}$, not direction, and is also symmetric with respect to the $E = 0$ plane. The low energy dispersion relation of equation (4) is also known as the Dirac cone, which is plotted in figure 2b. The Dirac cone is often used to describe the electronic properties of graphene and it is also the basis of the analysis of the phenomenon related to conduction in this thesis.

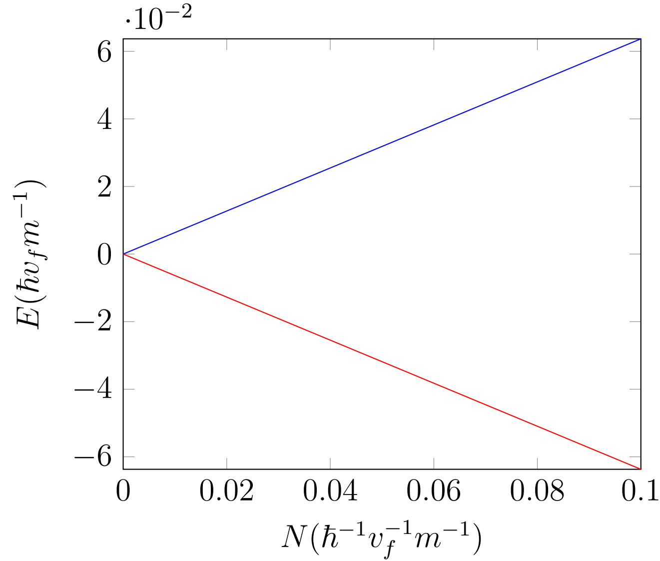

Figure 3. The density of states for in the vicinity of a Dirac point. The blue line is for conductance band states and red is for valence band states.

The density of states (DOS) is a material property that is used to describe the number of states at electrons for an energy level, or how many electrons can occupy the energy level. In graphene the low energy dispersion leads to a linear relation between $|E|$ and the DOS. This can be calculated by using the two dimensional density of states:

$$N(E) = \frac{1}{A}\sum_k \delta(E - E(k)) = n_{dg}\frac{1}{A}\frac{A}{(2\pi)^2}\int 2\pi k \mathbf{d}k\delta(E - E(k)), \tag{5}$$

where the n_{dg} takes into account the possible degeneracy of states and A is the unit cell area. Now taking equation (4) one can write $|\vec{k}|\mathbf{d}|\vec{k}| = \frac{|E-\mu_g|\mathbf{d}|E|}{\hbar^2 v_f^2}$ and equation (5) can be used to calculate the density of states in graphene:

$$N(E) = n_{dg}\frac{1}{2\pi}\int \delta(E - E(k))\frac{|E|\mathbf{d}|E|}{\hbar^2 v_f^2} = \frac{n_{dg}|E|}{2\pi\hbar^2 v_f^2} = \frac{2}{\pi\hbar^2 v_f^2}|E| = \alpha|E|, \tag{6}$$

where $n_{dg} = 4$ takes into account the two fold spin degeneracy and the two fold valley degeneracy (eq. (3)) and $\alpha = \frac{2}{\pi\hbar^2 v_f^2}$ is a constant. The density of states at fermi energy is zero and has a linear relation with respect to $|E|$ (fig. 3). The density of states in equation (6) explains the zero gap semiconductor and semimetal references for graphene as it predicts a zero DOS at the fermi-energy but there is no real gap between the valence and conductance bands. The low density of states in the vicinity of fermi energy results in some semiconductor like properties. For example graphene can be doped by extrinsic

sources and the majority charge carriers are different depending on the effective doping of the graphene, as described in figure 4. The missing band gap however means that there is no clear insulating state, but there still is a charge carrier minimum at the $E = 0$.

In addition to the single layered graphene also double layer and multilayer graphene are commonly observed in chemical vapor deposition based samples. In multilayered material the stacking graphene sheets are bound weakly by van der Waals forces and the electronic band structure is different than in single-layered graphene and the stacking geometry also affects the band structure [19, 20]. The band structure of AB-stacking bilayer graphene has overlapping non-linear conduction and valence bands [20] and is metallic in nature but asymmetry in the energies of electrons in the layers can open up a gap that can be controlled by an electric field [19]. In both cases bilayer graphene has a charge carrier minimum at the $E = 0$ and in that regard is similar to single layered graphene.

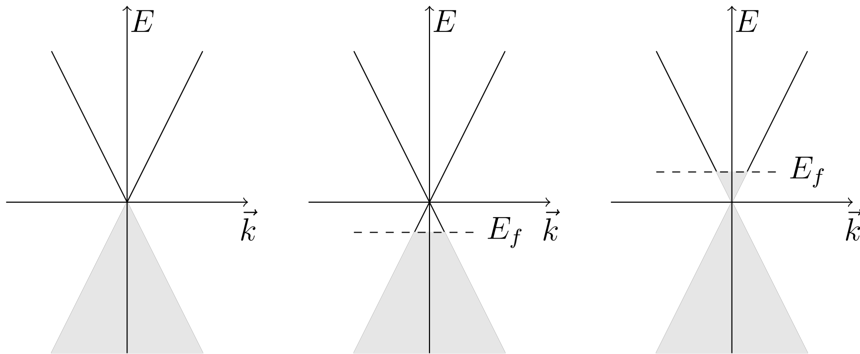

Figure 4. The filled states of graphene in the projected Dirac cone. On the left image the graphene is undoped and fermi-level is at the Dirac point. In middle graphene is postively charged, ie. p-type doped, and the fermi-level is below the Dirac point. On right graphene is negatively charged, ie. n-type doped, and the fermi-level is above Dirac point.

2.2 Conductivity of a graphene junction from idealized model

A simplified circuit diagram of the static situation considered in this chapter can be seen in figure 5 in which the graphene device on the silicon oxide is considered as contact resitors R_c, channel resistor R_{ch} and the back-gate capacitor C_g. This section will present approximations and a simplified model for the effect of the different contributions to total device resistance.

The graphene channels fabricated and measured in this thesis are in the micron scale and in this length scale the conductivity of the channels can be describe by diffusive currents modelled by Drude conductivity. The graphene devices also include the metal contacts and at the contacts current is transmitted from metal to graphene and the effects of this transmission come also into play. The metal contacts have been evaporated on to the graphene and are in near contact with graphene separated by thin vacuum (no covalent bonding) gap where conductance from the contacts to graphene is ballistic.

The density of states plays a crucial role in determining the conductance of both the channel and contacts. The concentration of charge carriers at finite temperatures is

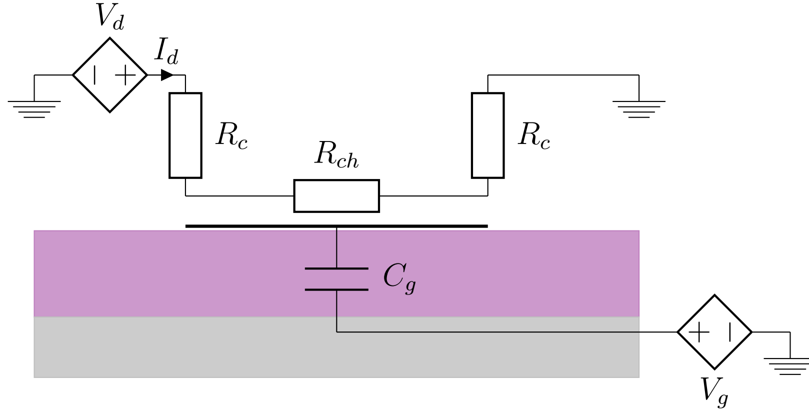

Figure 5. Simplified circuit for a graphene device defined by contact resistance R_c, graphene channel resistance R_{ch} and gate capacitance C_g.

calculated from:

$$n = \int_0^\infty \mathbf{d}EN(E)f(E) \text{ and } p = \int_0^\infty \mathbf{d}EN(E)(1 - f(E)), \tag{7}$$

for the electrons (n) and holes (p). Here $N(E)$ is the DOS in equation (6) and $f(E,T) = (1+e^{\frac{E-E_f}{kT}})^{-1}$ is the fermi distribution defined by T temperature, k boltzmann constant and E_f the fermi level. For graphene at non-zero kelvin temperatures the fermi distribution means that the current is carried by both p (holes at valence band) and n (electrons at conductance band) type carriers in the vicinity of the fermi energy. For sake of simplicity I have used the fermi distribution at zero kelvin ($f(E,0) = \delta(E)$) and one just has to remember that the temperature results in higher charge carrier density especially in the vicinity of the Dirac point. The density of charge carriers (n or p) with this approximation depending on the sign of fermi-level is:

$$\rho = \int_0^\infty \mathbf{d}E \frac{2}{\pi\hbar^2 v_f^2}|E|\delta(E) = \frac{2}{\pi\hbar^2 v_f^2}|E_f|, \tag{8}$$

where the linearity of DOS leads to linearity in charge carrier concentration. In addition to the thermal effects also the disorder in the graphene will cause intrinsic doping, non linear effects in the density of states and also an increase in scattering induced by the disordered states [21, 22].

The semiclassical conductivity for the graphene channels can be written as:

$$\sigma = e\rho\mu = e\mu\frac{2}{\pi\hbar^2 v_f^2}|E_f| \tag{9}$$

where the charge carrier concentration ρ is from (8) and μ is mobility of the charge carriers which can also be limited by scattering. The conductivity in equation (9) is linearly dependent on the fermi-level of the system.

The measurement geometry of figure 5 includes also a gate capacitor with C_g as capacitance per area and this capacitor can be charged by gate voltage V_g. The charging

per area (Q/A) of a common planar capacitor can be written as [1, 23]:

$$Q/A = \frac{C_g}{e} V_g \propto E_f, \tag{10}$$

resulting in a shift of the relative position of the fermi-level with respect to the bands, which allows electrostatic doping of the graphene device.

In addition to the channel resistance the model for the simplified circuit in fig. 5 also includes the contact resistors R_c. The charge carriers have to transmit over the thin contact gap between the graphene and metal electrodes ballistically. The conductance of a ballistic junction can be written as:

$$C = \frac{h^2}{e} \sum_i^M T_i, \tag{11}$$

where M is the total number of available modes, T_i is the transmission probability for a mode, e is the charge of the charge carriers and h is planck's constant. The number of modes depends on the density of states which is large for a metal and low for graphene and this means that the number of modes is limited by the modes of graphene $M_g(N)$ [24]. Assuming the same transmission for each mode $T_i = T_g$ the ballistic conductance for graphene-metal (C_{gm}) junction takes a form dependent on the density of states:

$$C_{gm} = \frac{h^2}{e} M_g(N)T. \tag{12}$$

There is a large variation in contact resistances for different metals and the lowest contact

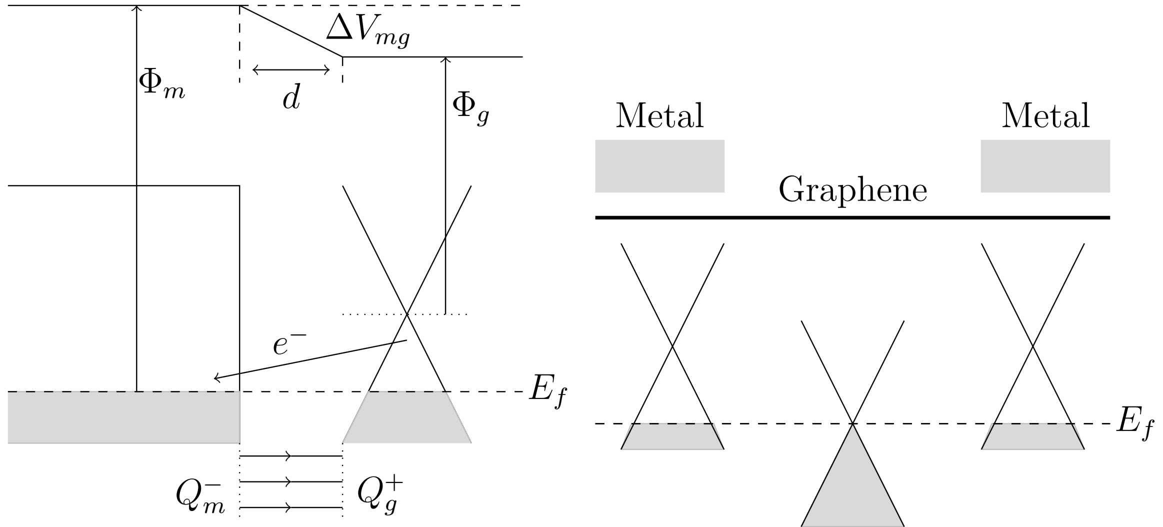

Figure 6. On the left doping of graphene in contact with metal with higher work function $(\Phi_m > \Phi_g)$. Graphene is charged positively so that the change in fermi level E_f, the potential difference ΔV_{mg} induced by charge difference $|Q_m^+ - Q_g^-|$ and the work function of graphene Φ_g correspond to the metal work function Φ_m. The d is corresponds to the vacuum gap between metal and graphen at the contact. On right an illustration on the fermi level of graphene in a pristine graphene sample contacted by metal with higher work function.

resistances are observed in metals such as Pd and Ni with high work function [24]. This is

related to the charge transfer between the metal and graphene which is described in figure 6 [25]. A metal with high work function in contact with graphene $\Phi_m > \Phi_g$ result in high p-type doping and thus results in a higher hole type charge carrier density as in graphene described in equation (5) which results in a higher $M_g(N)$ and conductance in eq. (12). The electrostatic doping of the graphene at contacts by a gate capacitor can be largely countered by a metal with high work function and in this thesis: $R_c(V_g) \approx R_c$ i.e. contact resistance is constant with respect to gating [26].

The doping profile at the edge of the contacts to channel form p-p' and p-n junctions due to high doping of graphene by nickel. The behaviour of $p - p'$ and $p - n$ junctions in graphene is different than that of a common diode. Due to the chiral nature of massless Dirac fermions in graphene, the charge carriers can tunnel trough these potential barriers [7,27]. This tunneling is dependent on the angle of incidence of the charge carriers. Based on the work of M. I. Katsnelson et al. 2006 [7] it seems that the charge carriers in graphene can tunnel with near unity probability trough these junctions if the incidence angle is perpendicular or close to perpendicular and also for a few other angles. Depending on the distribution of the angles of incidence, the potential barrier at the edge of contact can be nearly transparent for the charge carriers but the transmission propability is still lowered atleast slightly by the formation of these junctions.

The contact resistance by earlier considerations is close to constant R_c and only the channel resistance is modified by the gate voltage. Combining this assumption with the results of equations (9) and (10), the conductance in the vicinity of the dirac point has a relation:

$$G \propto |V_g|, \tag{13}$$

a linear dependency for the total junction conductance G on $|V_g|$, where $V_g = 0$ would corresponds to the conductance minimum when the fermi-level is at the Dirac point. In many systems the initial charge on graphene and interaction with the environment will cause additional effects that leads to non-linearity in the transfer characteristics ($G(V_g)$). The next section will discuss more about the considerations of the graphene devices as part of a measurement circuit and environment.

2.3 Graphene in a measurement setup

The electrical measurements in this thesis were used to measure the conductance of the graphene devices and the dynamic response of the conductance to the electrostatic doping caused by applying a gate voltage. The conductance measurements are done by measuring the current I_d with respect to bias voltage V_d by two-probe measurement circuit represented in figure 7a and four-probe measurement circuit in figure 7b. The V_g in the figures corresponds to the gating voltage. In two-probe measurement the channel voltage is measured from the bias electrodes by connecting a differential voltage amplifier in parallel with the graphene device ($V_d \approx U_d$). The two-probe resistance of the system is:

$$r_{2-p} = \frac{V_d}{I_d} = ((r_{w1} + r_{c1} + r_{ch} + r_{c2} + r_{w2})^{-1} + (r_{ampf})^{-1})^{-1} \approx r_{c1} + r_{ch} + r_{c2}, \tag{14}$$

where the r_{w1} and r_{w2} are the resistances of the wiring and instruments, r_{c1} and r_{c2} are the contact resistances, r_{ch} is the resistance of the channel and r_{ampf} is the resistance of the voltage amplifier. The approximation in the end notes that the r_{ampf} is often several orders

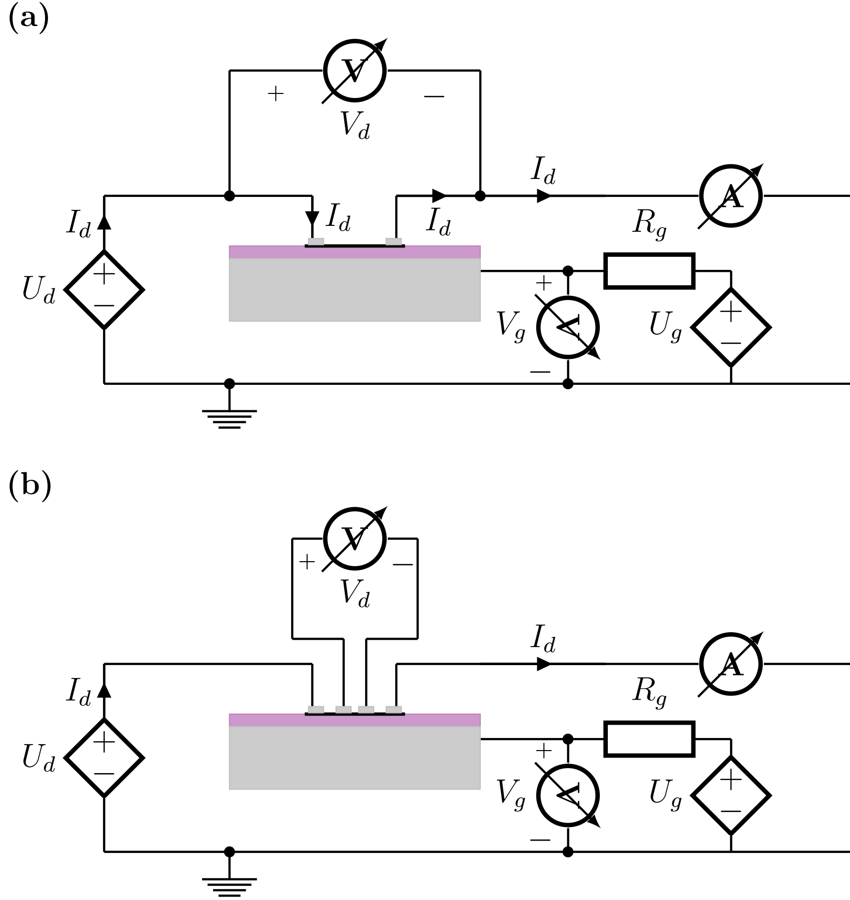

Figure 7. The two- and four-probe measurement circuits for graphene devices. The measurements of drain voltage (V_d) and drain current (I_d) include also amplification schemes. **(a)** Two probe measurement system for graphene devices. The voltage is measured at the source and prior to current amplifier which acts as a virtual ground and is used to measure the drain current. **(b)** Four probe measurement system for graphene. The voltage is measured from the additional electrodes on the graphene placed between the voltage appliance and grounding electrode.

of magnitude larger than the other terms in the equation and the resistance of wiring is much smaller than the contact resistance. With these approximations the two-probe resistance r_{2-p} includes the resistance of the contacts and the channel. The four-probe measurement is done by measuring the channel voltage from additional electrodes between the bias electrodes on the sample. The voltage V_d depends on the current going trough the whole sample and the resistance of the channel between the measurement elecrodes. The four-probe resistance can be written as:

$$r_{4-p} = \frac{V_d}{I_d} = (((r_{w1} + r_{c1} + r_{ampf} + r_{c2} + r_{w2})^{-1} + r_{ch}^{-1})^{-1} \approx r_{ch}, \tag{15}$$

where the r_{c1} and r_{c2} are the contact resistances of the measurement electrodes, r_{ampf} is the resistance of voltage amplifier and r_{ch} is the channel resistance. The same approximation about the r_{ampf} as in case of r_{2-p} can be done to conclude that the r_{4-p} corresponds closely to the resistance of the channel. Comparison of the two-probe resistance (14) and

four-probe resistance (15) can be used to solve the contact resistance:

$$r_{2-p} - r_{4_p} = r_{c1} + r_{c2} = R_c. \tag{16}$$

The contacts have metal overlapping with graphene which can effect the properties of the devices.

The figure 8 shows resistor network models for two-probe and four-probe measurements. The resistivity of the electrode material is lower than the resistivity of the graphene, which means that the path of the least resistivity goes through the edge of the contact. This means that the current density should be highest at the edge as illustrated in the figure 8a. The transfer lengths of the contact could be determined with the resistor network model, however the density of states limited ballistic transport at the metal-graphene contact means that the applicability of the model to determine the transfer-lengths as in normal semiconductor metal junctions is questionable [24].

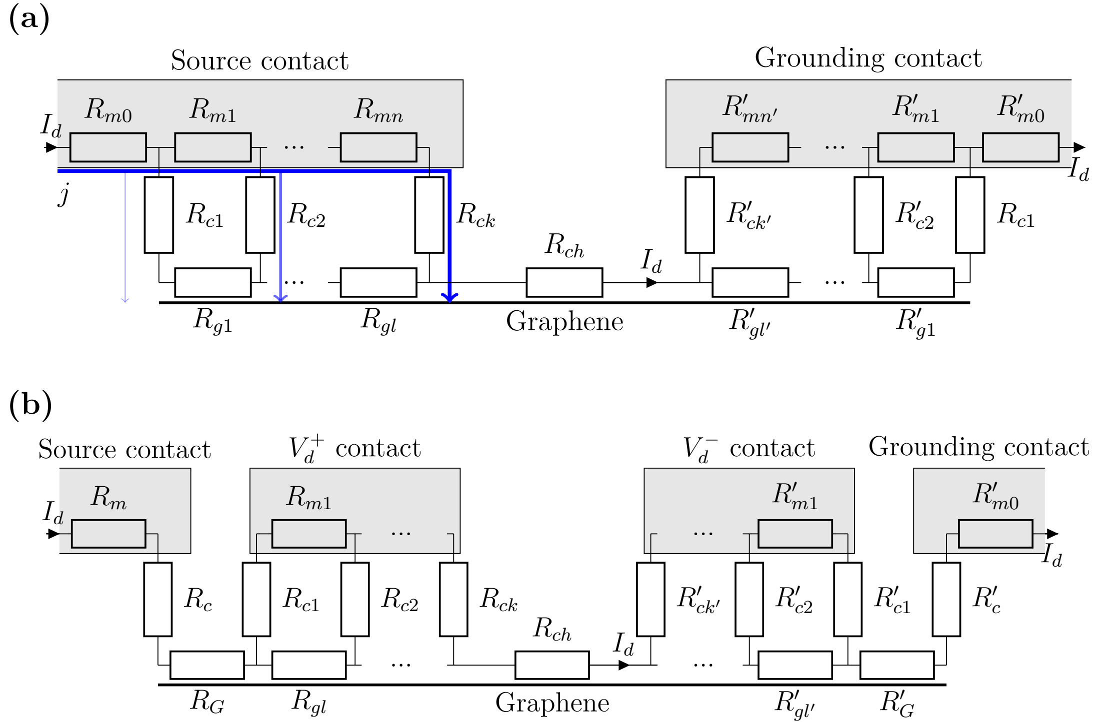

Figure 8. The resistor network models for contacting graphene devices. **(a)** A resistor network model for two-probe contacted graphene with a constant fermi-level. The blue arrows describe the intuitive behaviour of current density trough the contact junction. **(b)** A resitor network model for four-probe contacted graphene with a constant fermi-level. R_c and R'_c are simplified from the case of a), even though same considerations still apply to them.

The model works though for general considerations of the contacts and it can be concluded that increasing the area of metal in contact with graphene is not as important as increasing the contact width in the minimization of contact resistance. Figure 8b illustrates the problem of probing the voltage with non-neglible width of metallic measurement contacts on graphene: How is the V_d^+ and V_d^- determined by the contacting and channel geometry? Perhaps the point is closer to the outer edges of the contacts with the resistors

R_{c1}, R'_{c1}, but in order to minimize the headache I have decided to use the middle points of the measurement electrodes since no large scale statistical analysis of the contact resistivity was conducted. The determination of contact resistances done in the measurements is used to get a better idea on the relative magnitude of resistances for the measurement geometry.

The electrostatic doping of the graphene devices is done by applying a sweep with the U_g-source for both two-probe and four-probe measurements as shown in the figure 7. The linear dependency of the conductance to gating voltage in equation (13) needs also a constant charge term $n_0 e$ (initial doping) and more dynamic charging factors $n_\Delta(V_g(t), T, p, c(\mathrm{H_2O})...)$ dependent on the prior gating $V_g(t)$, temperature T, pressure p, humidity $c(\mathrm{H_2O})$ and possible other factors which are dependent on the environment [28]. The constant charge present on graphene shifts the dirac-voltage (charge neutrality point) from $V_g = 0$ to $V_g = V_{Ef}(n_0 e)$ resulting in $G \propto |V_g - V_{Ef}(n_0 e)|$. The dynamic charge is mostly added to the graphene by charge traps excited by V_g and atmospheric charged absorbed particles countering the charging by V_g resulting in a shift of the charging voltage $V_{ex}(V_g(t))$. Assuming that the mobility and the band structure remains mostly unaffected, the conductance is:

$$G \propto |V_g - V_{Ef}(n_0) - V_{ex}(V_g(t))|. \tag{17}$$

The result of this function assumes that the the density of states has still a linear relation, but the initial charge and the measurement environment can add additional terms to the electrostatic charging by gating voltage and thus resulting possibly in a non linear relation between G and V_g. What are the limitations of $V_{ex}(V_g(t))$? Assuming that there are no abrupt changes in the system, where for example a large change in surrounding humidity causes a change in the adsorption rate vs desorption rate for water molecules, the charging is limited to counter charging. This means that the charging caused by V_g is countered partially by opposite charge and even if the total charging $Q(t)$ during applied unidirectional $V_g(t)$ is not linear, $V_{ex}(t)$ should not result in change of the sign in charging: $|dQ_g(V_g(t))/dt| - |dQ_{ex}(V_{ex}(t))/dt| > 0$. The relation in (17) models the behaviour related to the charging effects due to electrostatic doping, but in the vicinity of the Dirac-point the temperature induced charge carriers and the non homogenous charge distribution dominate which give rise to different form to the relation [29].

The effects of the V_{ex} can be seen as less effective gating which shifts the conductance minimum and can include non-linear terms. This means that the transconductance of the system, defined as: $g_m = \frac{\mathrm{d}I_d}{\mathrm{d}V_g}$ when V_d is constant, is not constant or even symmetric in magnitude with respect to the charge carrier minimum. In the ideal case of equation (13) the transconductance would be a negative or positive constant depending on sign of V_g. It should also be noted that because graphene is a linear component ($G(V_d)$ is constant) the transconductance is just scaled with $1/V_d$ when bias voltage is changed ($dG/dV_g = g_m V_d^{-1}$).

Uneven doping of graphene results in areas with different charge carrier concentrations and can result in multiple charge carrier minima in the graphene devices each of which corresponds to a charge carrier minimum for an area. Lets consider two areas (A and B) of graphene with different initial doping n_{0A} and n_{0B} connected in series and k_A, k_B constants taking into account the possible differences in mobilities and geometries of the

areas. The conductance of the connected areas is related to the charging of the areas:

$$\frac{1}{G_A} + \frac{1}{G_B} \propto \frac{1}{k_A|V_g - V_{AEf}(n_{0A}) - V_{Aex}(V_g(t))|} + \frac{1}{k_B|V_g - V_{Ef}(n_{0B}) - V_{Bex}(V_g(t))|} \quad (18)$$

Equation (18) can give rise to multiple conductance minimas, that are the result of the charge carrier minima of the differently doped areas $V_g = [V_{Ef}(n_{0A}) + V_{Aex}(V_g(t)), V_{Ef}(n_{0B}) + V_{Bex}(V_g(t))]$. The dependency is again more an idealized version of the graphene devices and the dependency in the vinicity of the Dirac-points of the areas takes a different form [29, 30]. A rise in the conductivity of an area can overshadow a dip in conductance for other areas and no minimum in the overall conductance of the device is necessarily observed. The uneven doping of the graphene can create parallel conductors with slightly different V_{Ef} contributing towards a larger effective charge carrier concentration at the minimum and a higher minimum conductance.

3 Experimental methods

3.1 Sample fabrication: Chemical vapour deposition, transfer and device fabrication

The chemical vapour deposition of graphene can produce continuous large-area covering films of graphene [31]. However the films produced in CVD-processing consist of multiple islands of miss-aligned graphene flakes, defected graphene, folded graphene and multilayer domains but also large millimeter sized single crystalline growths have been reported [14]. The high quality of graphene is considered to be obtained by having a large grain size for the graphene islands and by having minimal defects and multilayered domains on the lattice. The goal of synthesizing high quality single-layer graphene by CVD is largely persued in the field of graphene studies as it can lead to a scaling method for providing the material for industry.

The basic requirements for the growth process are a carbon source, carrier gases, annealing gases, a catalytic surface and high temperature. The carbon source can vary from gaseous methanol, ethanol, propanol and methane to solid organic carbon sources [32–34]. The carrier gas is an inert gas used to create continuous flow trough the system and is commonly Ar. The annealing gases usually include also a carrier gas and and a small concentration of H_2 [35]. Two common catalytic metals used in the CVD of graphene are nickel and copper and especially copper has been used to synthesize decent quality large-area graphene [14, 31]. The high temperatures in annealing phase result in reordering of the lattice of the catalyst metal and formation of a more continuous growth platform for graphene. In the growth phase the high temperature is a requirement for decomposure of the carbon source.

The graphene growth mechanisms on nickel or copper surfaces are different: bulk mediated on nickel and surface mediated on copper. The difference of the mechanism between these metals is caused by the interaction of carbon and the metal lattice [36]. Carbon has a high solubility in nickel and after the precursor has been broken down, the carbon atoms diffuse into the bulk of the metal. In the cooling step the solubility of carbon is lowered and the carbon surfaces from bulk of the nickel and the carbon forms graphene on the nickel surface. This process produces often multilayered graphene as the concentration of dissolved carbon in the nickel lattice is hard to control and the already grown graphene does not limit the growth as well as it would in surface mediated process.

The solubility of carbon to copper is minuscule but carbon can diffuse along the surface and due to this the growth of graphene on copper is surface mediated. In the surface mediated growth carbon atoms diffuse mainly on the surface as different carbon species (monomer, dimers, trimers...) until nucleation and formation of graphene islands. The graphene grown on the surface prevents decomposition of carbon source which results in a self-limiting reaction. The number of forming growth islands for graphene per area is called the nucleation density. The lower nucleation density, atleast in theory, should lead to higher quality graphene as there are fewer grains (islands of graphene) and which results in fewer grain boundaries i.e. more continuous lattice [37]. The surface mediated growth mechanism is depicted in figure 9.

The nucleation of the carbon atoms can happen as carbon atoms collide on the surface forming heavier carbon molecules which continue to grow and form islands of graphene.

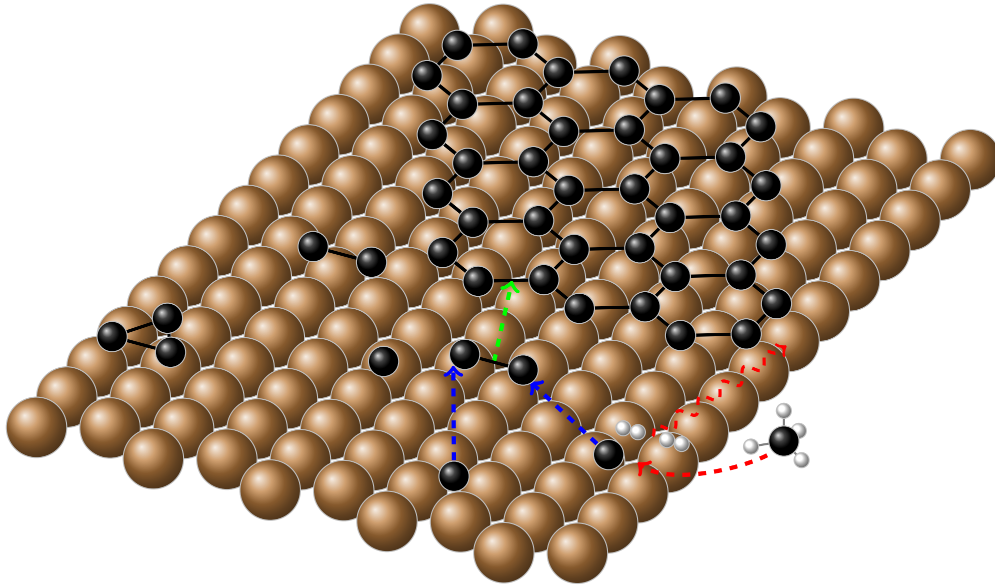

Figure 9. Simplified image of the surface mediated growth mechanism for graphene on copper using methane as the carbon source. The methane decomposes on the copper to carbon (red line) that forms dimer with another carbon atom (blue lines) and nucleates at edge of graphene (green line). The exact process of decomposition and formation of dimers and other carbon species is more complicated.

The nucleation can also happen at an impurity that binds carbon and forms a growth center or at a lattice imperfection which lowers the diffusion rate for carbon. The nucleation density works in determining the grain size of graphene in the growth process and limits the quality of graphene [37]. The lattice orientation can also effect the nucleation densities by resulting in higher diffusion along some directions [38].

The lattice constant of copper at (111) facet accommodates graphene lattice with small strain compared to for example Cu(100) facet [39]. The lattice orientation also affects the preferred directions for diffusion and the initial shapes of growing graphene islands and the final grain size [38]. The domains of (111) oriented copper can be miss aligned with respect to each other and form domain boundaries which tend to cause heavy nucleation and formation of multilayered graphene. The formation of single orientation (111) lattice can be promoted by deposition of a thin copper film on a supporting substrate which works as a template in annealing step for the copper lattice. A suitable substrate for promoting Cu(111) oriented copper is basal sapphire $\alpha - Al_2O_3(0001)$ and it also survives the high temperature neccessary in the growth of graphene [40]. This method relies on thin films of copper and the durability of this catalytic thin film is also important in the synthesis. Impurities in and on the copper and on the sapphire substrate can cause dewetting spots , i.e. formation of holes, and the parameters used in the deposition of the thin films can also have a notable effect in the final product [40].

Annealing of the catalytic surface prepares it for the growth by promoting the single lattice domain sizes and also diffuses H_2 into the copper lattice which promotes the uniformity of graphene during synthesis [35]. The lattice reorientation requires high temperatures which also promotes the diffusion of gas into the lattice. The H_2 diffused in copper lattice during the annealing step will take part in the decomposition of the

carbon precursor and also etch the graphene islands slowly during the growth [35]. The uniformity is increased because the etching takes part at the edges and results in small and thin features etching faster which promotes formation of fewer but larger islands.

The grain size of graphene is dependent on the concentration of carbon precursor and H_2 in the growth gas mixture and a lower carbon concentration has been shown to help in producing larger graphene grains [14]. The lower concentration of carbon on the copper surface results in fewer collisions between carbon atoms or other species which results in a lower nucleation density. H_2 introduced in the growth gas mixture helps in the etching of the graphene islands and controlling the growth with the H_2 diffused into the lattice during annealing. H_2 can also promote defects in the graphene during the cooling phase [35]. The control over the concentration of precursor and nucleation density was an essential problem faced in the synthesis and the limiting factor in the quality of graphene in this thesis.

After being synthesized the graphene is a single atom layer thick film with low density of states covering the sea of free electrons: the catalytic metal surface. The applications of the graphene might require different substrates, such as dielectric substrate for electronic devices or an elastic substrate for flexible electronics. Rather than attempting to synthetize the graphene directly on these surfaces one can use transfer by depositing a polymer based supporting layer or scaffold on the graphene and etching of the catalytic surface [41]. The stack of polymer/graphene can be then cleaned in baths of water and hydrochloric acid and then captured on the target substrate. In this process the final substrate is limited mainly by the adhesion of graphene and the chemical compatibility with the solvent used to remove the supporting layer.

The transfer can be a limiting factor in graphene quality as it can result in polymer residues, defects caused by the etching processes and folding of graphene [42]. The impurities decrease the mobility of the electrons, add charge to the graphene, increase the contact resistance and can also act as charge traps which hysteresis effects in field effect devices [42–45]. The addition of impurities by the transfer can prompt a need for cleaning steps such as annealing of the surface [45, 46] or different polymer free transfer methods such as the contact transfer [43]. Annealing is limited in its ability to clean the surface and can also result in lower mobility by promoting the interaction of the substrate and graphene [45].

The post-synthesis device processing of graphene can include steps to etch the graphene to wanted shape and size, addition of metal contacts, functionalization of the graphene and suspension of graphene in air. As a two-dimensional material, the quality of graphene is very vulnerable to surface contaminants and defects that can be caused by the device fabrication. The common lithography methods used to create micro- and nanoscale patterns include deposition of resists that can add to surface contamination of graphene and the etching steps can cause defects at the edges of etched graphene patterns. The adhesion between materials, such as the adhesion of graphene and substrate or graphene and electrode metal plays a large role in the success of device fabrication.

The etching of graphene to define the device structure can be achieved by using laser or ion based etching methods such as a focused beam of helium or neon ions or reactive ion etching and plasma etching by O_2 based methods [47, 48]. The focused laser and ion beam methods do not require masking but cannot be done in parallel for large areas. The plasma etching can be done as a parallel process but requires a mask. The fabrication of the masks

can be done by directly writing the etch pattern by scanning electron microscope on resist deposited on the graphene or by photolithography. In both of the cases the interaction of the deposited resist and graphene are crucial in determining the device quality in similar manner as in the transfer. The removal of the masks without damaging the graphene or delaminating can be tricky [42, 49]. In addition the resists are often also etched by the oxygen plasma and the etching can lead to poorly defined edges. The processing can be improved by using positive lithography and deposition of metal mask on the graphene [49]. In this case the area of graphene and resist on top of it is exposed which makes the process to remove resist softer and the metallic mask is more resistant to the oxygen plasma etching. The device fabrication method introduced in this thesis is a modified version of the metal masking method introduced by Kumar et al. 2011 (ref [49]). The method is modified by adding an interfacial copper layer between the initial steps of the mask patterning and remove the nickel mask only after the last patterning in order to avoid any additional resist residues on graphene after the transfer.

3.2 Materials and methods: graphene synthesis and device fabrication

The steps of the synthesis and transfer of graphene are depicted in figure 10. The synthesis was done on copper thin films deposited on chips (5 mm×5 mm) of polished $\alpha-Al_2O_3(0001)$. The sapphire substrates were cleaned by brushing the surface with a cotton stick in acetone and then rinsed in IPA. The cleaning of the surface was finalized with O_2 plasma: 120 s, 20 W, 30 mT in O_2. The deposition of copper was done by electron beam evaporation from 99.999 % pure copper source in pressure range of $1 - 3 \times 10^{-5}$ mbar and with a deposition rate of $0.5 - 5\,\text{Å}\,\text{s}^{-1}$. The resulting film thickness is in the range of 500 nm − 650 nm. The copper substrates were stored in N_2-cabinets in cleanroom, sometimes for days before next steps.

The annealing and chemical vapour deposition of graphene were both done during the same run for each sample. The copper coated sapphire chips were loaded into the tube furnace either in a small quartz tube supported by metallic thermocouple loading rod (fig. 11a) or with a quartz loading rod (fig. 11b). The tube furnace has a loading lock that can be pumped and filled with the processing gases after pumping. The atmosphere of the furnace during annealing step consists of Ar and H_2 obtained by flows of 50/50 *sccm* at 800 − 1000 °C. The annealing of copper substrates was done for 10 − 20 min, depending on the run, 20 min for ethanol based and 10 − 20 min for methane based synthesis runs.

In the last minutes of annealing the temperature of the furnace was set to the growth temperature at 1000 − 1040°C and once the synthesis temperature was reached the carrier gas (Ar) and H_2 flows were set to the growth process: 400 − 500 *sccm* of Ar and 20 *sccm* of H_2. The growth period was begun by opening the valve for carbon precursor to enter the furnace. The precursors used in this study were liquid ethanol and gaseous CH_4. The liquid ethanol was added by bubbling a low flow of Ar/H_2, 20/20 *sccm* through the liquid ethanol. The flows of the methane were in the range of 2 − 5 *sccm*. The growth period lasted from 5 min for ethanol to 6 − 20 min for methane after which the valve for precursor and H_2 was shut and the Ar flow was set to 100 *sccm*. After the synthesis samples were stored in ambient air for hours or days prior to deposition of transfer PMMA and examined under optical microscope (Olympus BX51M). Chosen samples were also imaged with

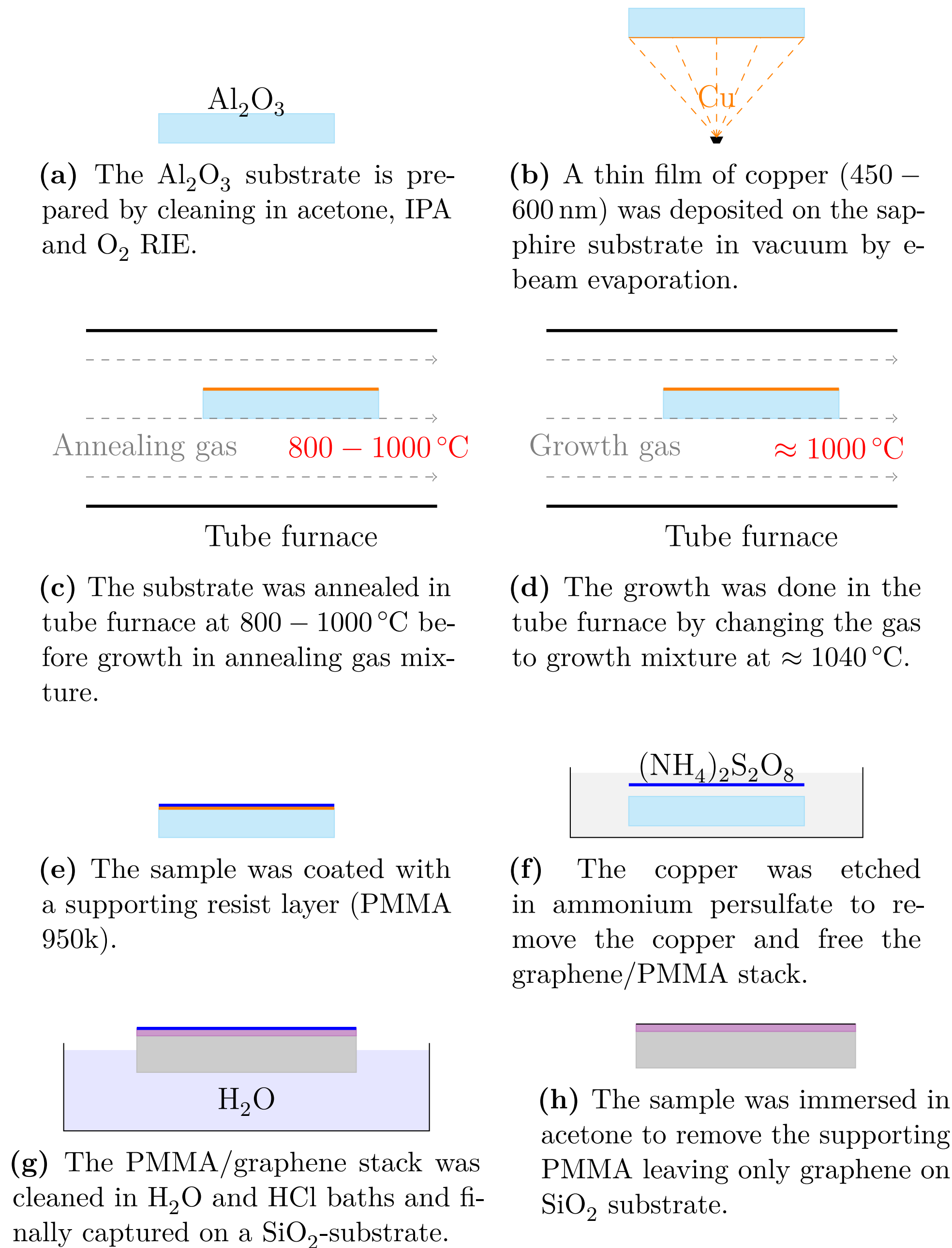

(a) The Al_2O_3 substrate is prepared by cleaning in acetone, IPA and O_2 RIE.

(b) A thin film of copper (450 – 600 nm) was deposited on the sapphire substrate in vacuum by e-beam evaporation.

(c) The substrate was annealed in tube furnace at 800 – 1000 °C before growth in annealing gas mixture.

(d) The growth was done in the tube furnace by changing the gas to growth mixture at ≈ 1040 °C.

(e) The sample was coated with a supporting resist layer (PMMA 950k).

(f) The copper was etched in ammonium persulfate to remove the copper and free the graphene/PMMA stack.

(g) The PMMA/graphene stack was cleaned in H_2O and HCl baths and finally captured on a SiO_2-substrate.

(h) The sample was immersed in acetone to remove the supporting PMMA leaving only graphene on SiO_2 substrate.

Figure 10. The steps of synthesis for graphene on copper thin film and transfer to insulating substrate.

scanning electron microscope (Raith Eline).

The transfer polymer was deposited on the graphene/copper/sapphire chip by spinning PMMA 950k A3 at 1.5-3k rpm for 45 – 60 s and baked for 2 min on hot plate at ≈ 160 °C, resulting in a ≈ 300 nm – 100 nm thick supporting layer. The sample was left in ammonium persulphate ($(NH_4)_2S_2O_8$) for 1 – 3 d to etch the copper and obtain the free-standing PMMA/graphene stack. After etching, the stack was transferred to a glass beaker of water and again to an another glass beaker of water and then to a cup of 12 % HCl and then again via two glass beakers of water. After cleaning, the stack was captured on a SiO_2

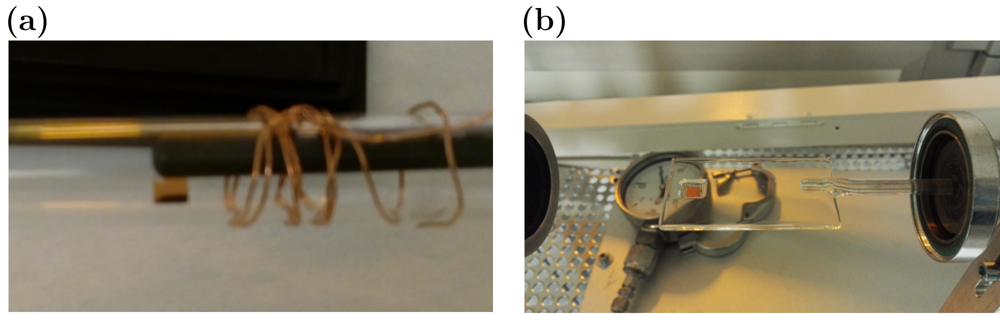

Figure 11. The loading supports of the catalytic copper/sapphire to the tube furnace. **(a)** Metallic thermocouple loading rod supporting a small quartz tube. **(b)** The quartz loading rod.

substrate, lifted from the water and heated for few minutes on 80 °C hot plate to remove water and promote adhesion. The finalization of the transfer was done by immersing the PMMA/graphene/SiO_2 stack to acetone for a few minutes to remove the PMMA layer.

The fabrication of metal contacted graphene devices was done in two different ways in this work. One way used prefabricated electrodes (5 nm of Ti and 30 nm of Pd) on silicon oxide substrate after which the graphene was synthesized from ethanol and transferred as described earlier without removal of the PMMA. After this the transfer PMMA was patterned to make the device geometry and disconnect the electrodes. The patterning was done by a Raith eLine scanning electron microscope with 30 µm aperture, 300 $\mu A\,s\,cm^{-2}$ dose and 20 kV acceleration voltage. The resist was developed in 1:3 MIBK:IPA developer for 45 s. The graphene was then etched by soft O_2 plasma etching (15 s, 20 W, 30 mT) and the PMMA was removed in warm acetone and annealed at 300 °C in N_2 atmosphere.

The process of metal mask based device fabrication by avoiding resist - graphene contact is seen in figure 12. The graphene on silicon dioxide substrate (fig. 12a) used in the processing were obtained from either Graphenea [50] or by in-house graphene synthesis. The first step of the processing was to deposit $20 - 30$ nm of copper on graphene and then deposit the resist on top of it. The deposition of metal was done by e-beam evaporation at a pressure of $1 - 3 \times 10^{-5}$ mbar and a rate of $1\,Å\,s^{-1}$. A bilayer of resists, PMMA 495k A3 as bottom layer and PMMA 950k A3 as top layer, was deposited on the copper by spinning at 3000 *rpm* and baking the PMMA 495k for 2 min and PMMA 950k for $2 - 5$ min on hot-plate at 160°C. The state of a sample after these processing steps is seen in figure 12b.

The mask pattern to define the graphene devices was exposed by Raith Eline with 30 µm aperture, 300 $\mu A\,s\,cm^{-2}$ dose and 20 kV acceleration voltage and developed by 1:3 MIBK:IPA for 45 s (see fig. 12c). The sample was etched in ammonium persulfate ($(NH_4)_2S_2O_9$, 125 $mmol\,l^{-1}$) for $10 - 15$ s to remove the copper at the exposed areas (fig. 12d). After this, e-beam evaporation at $2 - 4 \times 10^{-5}$ mbar and with rate of $1\,Å\,s^{-1}$ was used to deposit 30 nm of nickel on the sample (fig. 12e). The lift off of the deposited nickel was done in warm acetone with slight agitation currents by needle syringe. The excess copper was etched by immersing the sample in $(NH_4)_2S_2O_8$ for a few seconds to finalize the nickel mask pattern on the graphene (fig. 12f).

The metal masked graphene was etched by O_2-plasma for 15 s, with 60 W and 40 mT (fig. 12g). After this step the surface was clean silicon dioxide with the graphene/nickel stacks as device stacks and as location markers. A PMMA bilayer was deposited on the

(a) At the beginning of the processing the graphene was on 300 nm of thermal silicon oxide on silicon.

(b) The graphene was coated with a thin film of copper (≈ 20 nm) and positive resist was deposited on the copper.

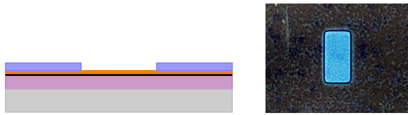

(c) The resist was exposed and developed by common e-beam (or light) lithography methods.

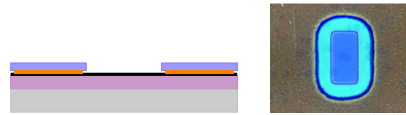

(d) The patterned sample was immersed in ammonium persulfate ($(NH_4)_2S_2O_8$) for short period of time (≈ 15 s) to etch the copper at patterned areas.

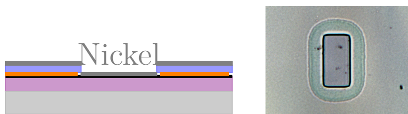

(e) A nickel thin film was deposited on the patterned sample to create a mask pattern for graphene.

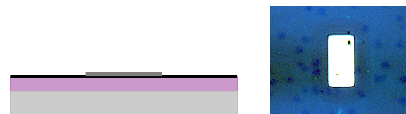

(f) The resist was lifted off in warm acetone and the excess copper is etched away in ammonium persulfate.

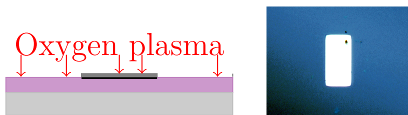

(g) The sample was etched by reactive ion etching with oxygen plasma.

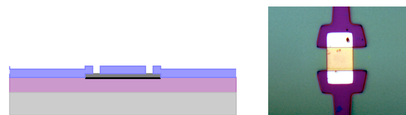

(h) A new layer of resist was deposited on the sample and the contact pattern was exposed on the sample.

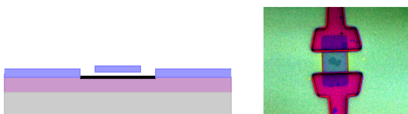

(i) The sample was immersed in HCL for $2 - 20$ h to etch the nickel mask.

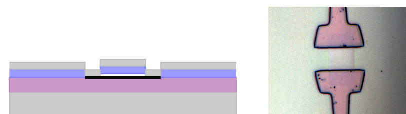

(j) The electrode metal was deposited on the sample by e-beam evaporation.

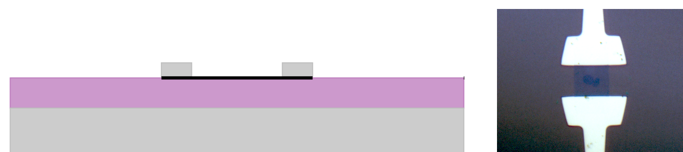

(k) The resist was lifted off to finalize the metal contacted graphene device pattern.

Figure 12. Metal mask processing of graphene devices with metal contacts by avoiding additional resist - graphene contact.

sample for electrode fabrication and during this step the nickel mask protected the graphene from contact with the resist. The deposition, exposure and development steps were done with same parameters as earlier. The graphene device with exposed electrode pattern on the resist is shown in figure 12h. The electrode patterning revealed also parts of the nickel mask and the sample was immersed in hydrochloric acid (HCl) with a concentration of $1\,\mathrm{mol\,l^{-1}}$ for $2-24\,\mathrm{h}$. The nickel mask is etched slowly at the exposed areas and also under the PMMA until removed (fig. 12i). The electrode metal, nickel or titanium/palladium, was deposited by electron beam evaporation with the same parameters as the mask earlier (fig. 12j). The lift-off was done in warm acetone as earlier with help of weak currents created by a needle syringe or by help of sonication. The finalized sample is seen in figure 12k.

3.3 Materials and methods for electrical measurements for pristine and femtosecond laser treated graphene

The samples used in the electrical measurements were fabricated by the device fabrication methods in earlier sections. The metal electrodes of the samples were connected to chip carriers with aluminium wire by supersonic bonding or directly by probes in a probe station. All of the instruments used in the measurements were controlled by a Labview program designed to form and measure DC-voltage sweeps.

Circuit diagrams for the two- and four-probe measurement geometries are presented in figure 7. U_d corresponds to the applied bias voltage across the sample and was controlled by a DAC-card (National Instruments BNC-2090). The applied bias-voltages ranged from 1 mV for pristine and more conductive samples up to 1 V for more resistive samples with defects or oxidization. Depending on the sample geometry the sample bias V_d was measured from the electrodes used to apply the bias voltage (two-probe system, 7a) or from the voltage probe electrodes (four-probe system, 7b).

The same basic measurement setup was used in all of the measurements with a few changes in parameters or additions of for example thermometers. The measurement of bias voltage was done by using a voltage preamplifier (DL Instruments 1211) with low-pass filter. The amplification was in each case so that the resulting amplified voltage would fit in range: $[-10\,\mathrm{V}, 10\,\mathrm{V}]$. The signal was grounded at current to voltage amplifier (DL Instruments 1201), which was used to measure the current and transform the reading into a voltage signal. As with the voltage amplifier, the amplification factor was set to $1 \times 10^3 - 1 \times 10^8$ so that the resulting signal would fit in the range of $[-10\,\mathrm{V}, 10\,\mathrm{V}]$. The voltage signals from the bias voltage amplifier and current amplifier were measured by the DAC-card. The gate voltage (U_g) sweeps were applied with a Keithley SourceMeter 2440 42 V or 2410-C 1100 V and measured with a Keithley MultiMeter 2001.

The measurement of transfer characteristics $G(V_g)$ of graphene devices vs. surrounding humidity were made in a probe-station with and environmental chamber. The chamber was connected to a Weiss humidity chamber which was used to control the humidity and temperature during the measurement. The humidity chamber was set to stabilize around a humidity set point and the feedback to the humidity sensor was provided from a humidity sensor in the measurement chamber. The temperature used in the humidity response measurements was set to 24 °C. A low-temperature measurement ($\approx 4.2\,\mathrm{K}$) was done in a dewar filled with liquid helium. A dipstick with sample chamber filled with gaseous

helium (20 mbar at 4.2 K) was inserted in the liquid helium and a resistor bridge was used to measure the temperature.

The femtosecond four-wave-mixing imaging (FFWM) and two-photon treatment of the samples for the thesis were done by Jukka Aumanen. During the treatment the samples were placed in a open-ended chamber that can be flushed with a flow of N_2 as depicted in figure 13. The samples were also connected to the electrical measurement setup and electrical measurements of the devices were done between the treatment cycles either under N_2-purge or in ambient air. The oxidization of the samples were done in air where the source of oxygen comes from air and the doping of the graphene was done under N_2-purge (no oxygen source). The FFWM and two-photon treatment of the graphene are basically identical processes except in FFWM the response signal of graphene is collected and the power of the pulse was usually lower. The laser setup used in the FFWM is depicted in appendix A. Some of the laser treated samples were imaged by Raith Eline scanning electron microscope and atomic force microscopy (Bruken Icon).

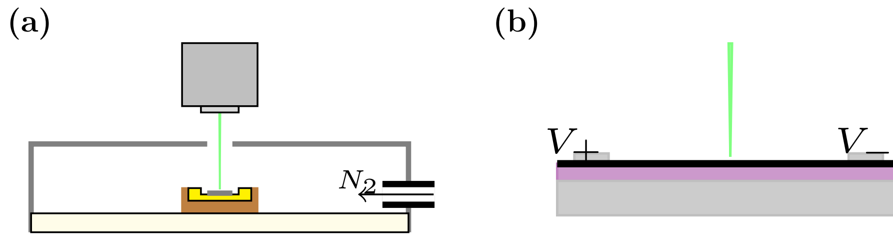

Figure 13. The treatment environment of the graphene. The sample is connected to a socket in the treatment chamber. **(a)** The laser treatment cycles were done in a open chamber with a possibility for N_2-flow on the side which was used in imaging and doping of the samples. The electrica measurements were done in the same chamber without removal immediately after the treatment cycles. **(b)** The laser is focused on the contacted graphene sample and exposed point by point or in case of lines as a single continuous sweep by moving the sample on piezo-stage.

.

4 Experimental results

4.1 The results of synthesis and device fabrication

The synthesis of graphene was completed for multiple samples with different parameters and loading schemes as described in the figure 10. The fastest way to get an idea on the graphene quality after synthesis is to use optical microscope to determine the quality of the copper substrate as it has effect on the nucleation density and the continuity of graphene. An optical comparison of three catalytic copper surfaces deposited on sapphire after annealing and growth are shown in figure 14. The copper surface in 14a has a large uniform domain with few dewetting spots, the surface of 14b has a high density of smaller copper domains and also higher dewetting density and the image in 14c shows a sample with domain size between the a) and b) but a high dewetting density. The metallic thermocouple was used in the loading for all of the three cases (fig. 11a) but the flow direction for the high dewetting point density in c) is opposite to a) and b). In the case of c) gas flow was directed from the direction of thermal rod (from right to left in fig. 11a) which may have resulted in a higher deposition of metal or other dirt particles from the metallic loading rod. The use of a quartz loading road (fig. 11b) removed the de-wetting and resulted in a more uniform growth platform for the graphene for the same flow direction as in 14c. Rigorous cleaning of the sapphire substrate did not have a noticeable difference on the dewetting which also points towards the fact that the deposition was added during the synthesis.

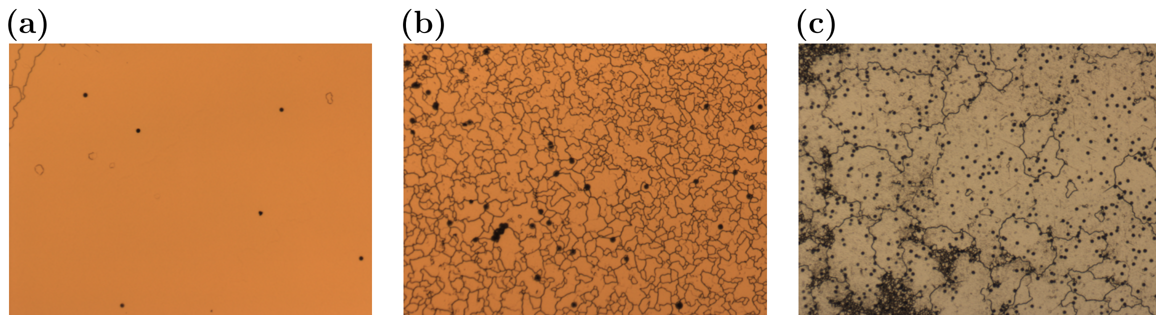

Figure 14. Comparsion of three different copper surfaces after annealing and synthesis. **(a)** Copper surface with minimal de-wetting and low copper domain density. **(b)** Copper surface with high copper domain density. **(c)** Copper surface with high de-wetting density.

The effects of dewetting were imaged with SEM on copper after synthesis and with optical microscope after the transfer, see figure 15. The SEM image shows a micron sized particle in the middle of the dewetting hole which may have caused the copper to withdraw during the heating. The withdrawing copper seems to have caused a circular wave-like features in the vicinity of the hole and shows that the effect of dewetting is extended beyond the hole. The optical image of the multilayer graphene synthesized on copper and transferred to SiO_2 shows the large discontinuity in the film caused by the holes and also additional PMMA residues surrounding the holes. A closer look at the optical image also shows darker regions at the edges of the dewetting points which may have been the result of additional nucleation and growth of graphene due to the edges of copper.

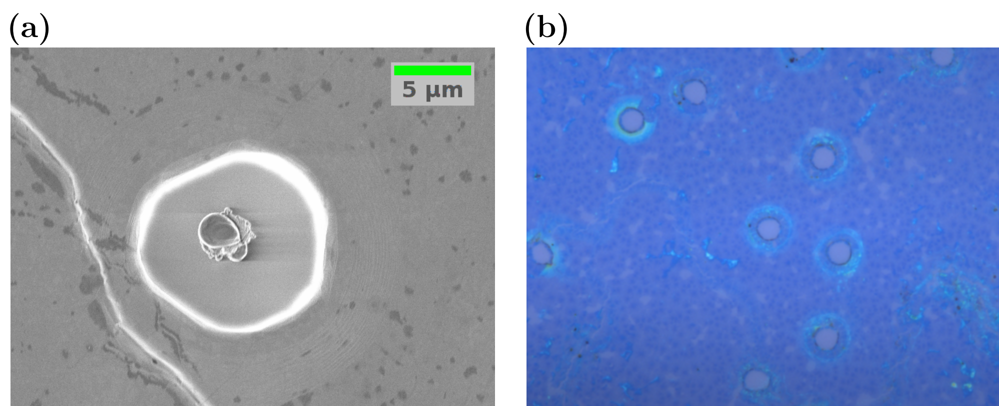

Figure 15. **(a)** SEM image of a dewetting spot on graphene/copper surface on sapphire after growth on left. The dewetting point causes circular wave-like effect that is extended further to the catalytic surface. **(b)** Optical image of multilayer graphene transferred on SiO_2 with dewetting points. The light-blue greenish color is caused by residual PMMA left-over from the transfer.

Figure 16a shows a SEM image of graphene which has grown in the vicinity of a copper domain boundary, where the orientation of the copper lattices next to each other does not match. The discontinuity of the surface has resulted in promoted nucleation during synthesis and in the SEM image this can be seen as darker areas of amorphous/multilayered graphene densely packed in the vicinity of the brighter lines, the domain boundaries of copper. The denser population of these domain boundaries can limit the growth of continuous single layered gains and increase the multilayer grain density.

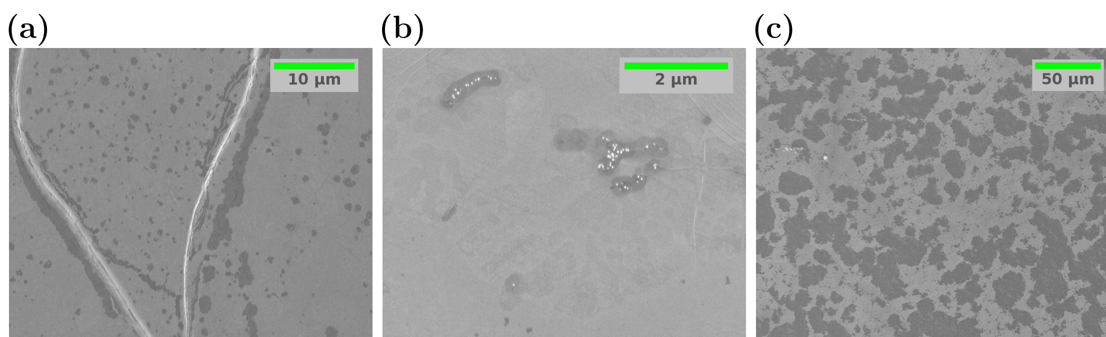

Figure 16. SEM-images of three different graphene samples on copper synthesized from ethanol with excess nucleation and formation of multilayer grains. **(a)** The darker multilayer grains are formed with higher probability at the boundary of copper domains with different orientation. **(b)** The small bright impurity particles have caused increase in the nucleation and formation of multilayer grains in the vicinity of the impurities. **(c)** Multilayer domains or/and amorphous carbon everywhere on the surface formed most likely by too high concentration of carbon in the system during growth or/and cooling.

Figure 16b shows a small area of homogeneous copper with bright white dots (impurities) and darker areas of multilayer graphene around them. These impurities have functioned as

nucleation centers during the synthesis and caused carbon crowding which has resulted in multilayer graphene. Figure 16c shows a uniform layer of copper with minimal impurities but still a high density of darker multilayer or amorphous carbon regions. In case of this sample the concentration of carbon in the growth was too high which has resulted in a carbon crowded catalytic surface.

The first carbon precursor for the synthesis of graphene was liquid ethanol added to the system by bubbling, i.e. directing a flow of argon trough the liquid. The correlation between the argon flow trough ethanol and the carbon concentration added to the furnace is hard to determine as the fluid dynamics involved are complicated and the carbon concentration might vary largely. Depending on the fill and state of the bubbler there might be a higher amount of evaporated ethanol already in the bubbler which may have resulted in higher initial concentration of precursor in the system. The SEM based analysis showed that synthesis using bubbler was poorly repeatable as similar parameters can result in graphene that is predominately poor quality and thick as in figure 16c or fewer domains of multilayer predominately at defects or domain boundaries as in 16a and 16b. Rather than trying to control the complicated fluid dynamics of bubbler to improve the repeability, the synthesis carbon precursor was switched to gaseous methane.

Using methane as precursor did introduce stability to the synthesis results but still fell short of the requirements for continuous single-layer graphene. Three scanning electron microscope images of methane grown graphene with different parameters are shown in figure 17. Figures 17a and 17b show graphene with few layers with dense snowflake like growths and figure 17c shows thicker dark regions that dominate the surface. The methane synthesis with the parameter range used did form more reproducible results and did not show large growths of amorphous carbon. This would suggest that the gaseous methane flow is more stable source for carbon but the formation of multilayer graphene would suggest that the concentration of was too high.

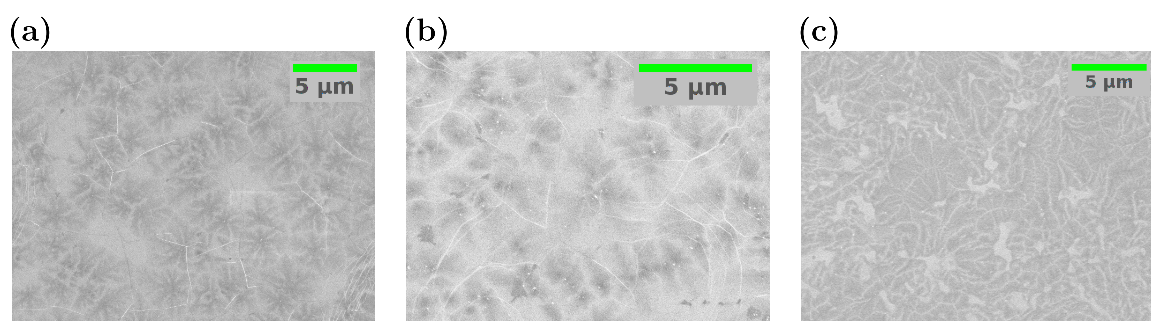

Figure 17. Results from graphene synthesis using methane. **(a)** Graphene grown with 5 SCCM for 6 min. **(b)** Graphene grown with 2 SCCM for 10 min. **(c)** Graphene grown 5 SCCM for 10 min.

The device fabrication was done by two different methods: premade electrodes and patterning the transfer PMMA or metal masking process (fig 12). The idea behind using the transfer PMMA as mask was to reduce the PMMA residues by avoiding additional deposition and baking of the resist directly in contact with graphene. In order to save time on exposure the devices were fabricated by exposing and etching only 1 µm lines around the measurement electrodes and the graphene device. Optical images after exposure and etching and SEM images after removal of PMMA of two different samples are seen in

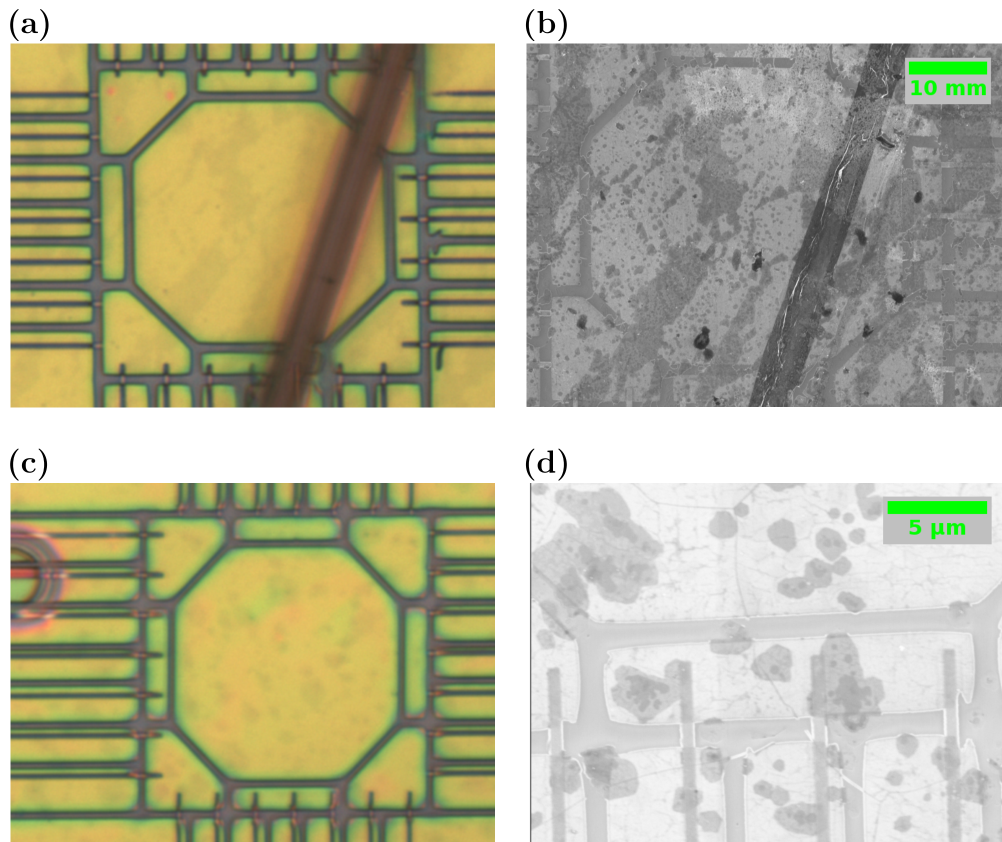

Figure 18. The transfer PMMA used as etching mask for graphene devices with pre-transfer fabricated electrodes on the substrate. **(a)** Transfer PMMA based fabrication. The device pattern has been exposed, developed and etched by oxygen plasma with 1 µm wide pattern. The dark line wide in the image is a fold in the transfer PMMA. **(b)** The same device as in 18a after removal of PMMA in acetone. There are alot of residues left and the fold results in thick unetched folded graphene strip. **(c)** A graphene device etched with transfer PMMA mask with 1 µm wide pattern. There is a bubble in the transfer PMMA on the upper left corner which has prevented the etching. **(d)** The lower middle device from 18c. The PMMA residues are seen on the graphene but the device is functional otherwise.

figure 18. The images show that the planar flatness of the transfer PMMA causes problems during the device fabrication. The success of e-beam lithography was limited by the visible fold in PMMA in figure 18a and by a bubble in figure 18c. The SEM images 18b and 18d shows that the transfer PMMA left considerable residues behind after the device processing.

The optical images in figure 12 show the results of different steps during the metal masking process. The copper deposited as the initial protective layer was chosen for two reasons: the graphene has already been in contact with copper and has already been etched in ammonium persulfate, which reduces the number of materials used in the whole process. Nickel was chosen for masking metal because it complimented the copper: the copper is etched fast by ammonium persulfate but nickel is barely touched by it, which was required in the processing step in figure 12f. Nickel also has higher adhesion to graphene than copper, with nearly 6× higher bonding energy per area [51]. Lastly nickel can be

etched in dilute HCl, preventing possible damage to graphene caused by stronger acids.

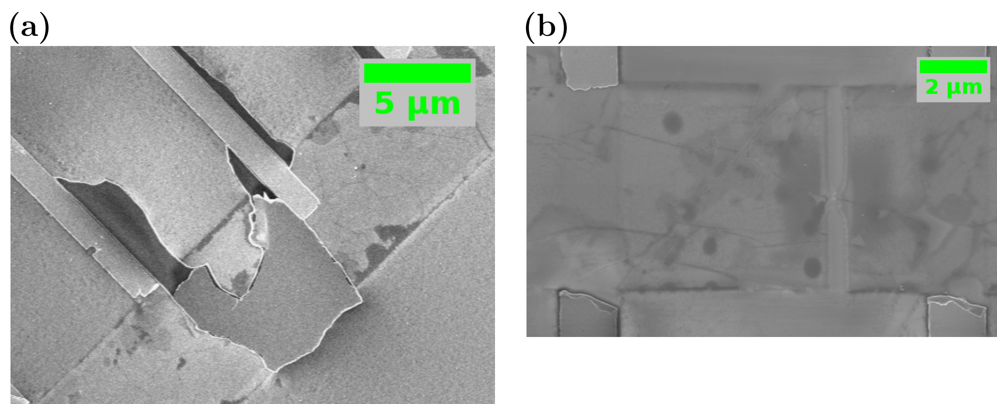

Figure 19. The weak adhesion of metal on graphene means that strong agitation in a solvent cannot be used in the fabrication process to finalize the lift-off. **(a)** Partially succesful lift-off leaves metal residues on the surface, which can be induced for example by uneven resist caused by dust particles on the surface during deposition of resist. **(b)** Electrodes (Ti/Pd) have delaminated off from top of graphene only, caused by sonication.

The main problem I came across during the metal mask processing was the lift-off of the metal/PMMA mask (step between 12j and 12k) after electrode fabrication. The electrode fabrication process creates often multiple features and the risk for damage such as seen in figure 19a is greater than in the metallization of the mask. The figure shows a metal strip connected between the electrodes which should have been prevented by the bilayer resist. However the residues gathered on the chip during the processing caused inconsistency in the thickness of the layers which results in poor local undercuts. Removal of the residues can be risky as the adhesion of the graphene/nickel mask stack to the silicon oxide is poor and most cleaning steps (rinsing, blowing) resulted in the delamination of markers and devices. In some cases agitation in a solvent was able to remove some of the flakes, however too strong agitation resulted in damage to the electrodes. In the case of figure 19b the sample was sonicated in acetone which resulted in multiple electrodes lifting off the graphene due to weak adhesion of metal to graphene.

The metal masking process employed for samples with little to no dust on the surface resulted in a working lift-off with soft agitation (no delamination) and no extra metal on the top. Example of a working device is shown in figure 20a, where there are no visible PMMA contaminants or large defects that could have been caused by the fabrication. Raman spectra of three different samples fabricate with this method are shown in figure 20b. The high D-peak/G-peak ratios (0.5-0.9) in the Raman spectra suggest that damage was induced to the samples by the processing. The oxygen plasma etching, etching of nickel or nickel residues may have contributed to the high D-peaks.

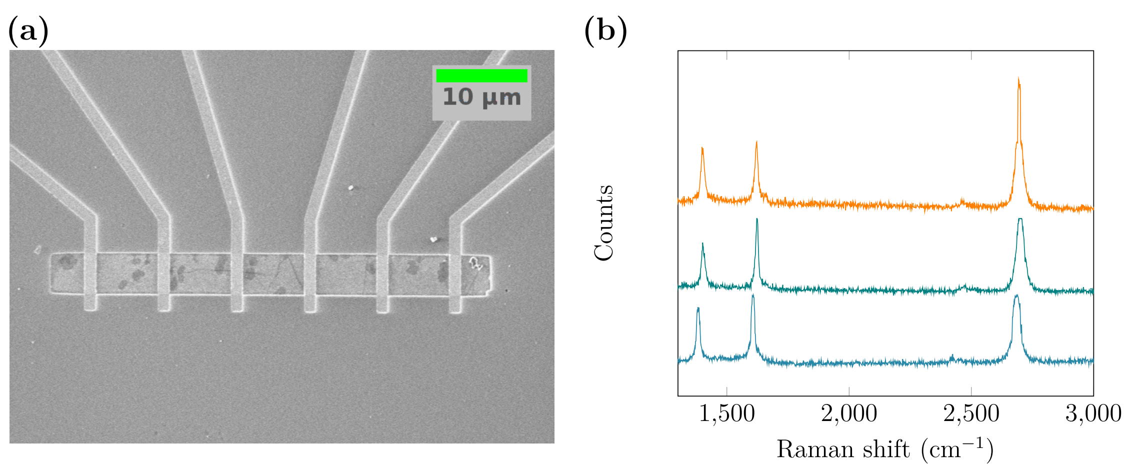

Figure 20. SEM-image of a device fabricated with metal masking and Raman spectra from three different devices. **(a)** A working example device fabricated with the metal masking process. **(b)** Raman spectra of graphene devices after metal mask fabrication. The tall peaks from left are D, G and 2D.

4.2 Resistance of graphene devices with two-probe and four-probe measurements.

The conductance (G) or resistance ($R = G^{-1}$) of graphene devices depends on the channel geometry, quality and fermi-level of the graphene. The graphene devices with constant gate-voltage can be considered as resistors with linear dependency between the drain voltage V_d and drain current I_d. The slope of $V_d(I_d)$ (or IV) corresponds to the conductance of a linear component and the resistance of graphene devices has been measured in this section by applying a V_d sweep and measuring the response $I_d(V_d)$. The intersection of the line can also be used to determine systematic error in V_d, if the current measurement has little to non systematic error. The geometries of different diffusive channels can be compared by using the number of squares in the channel, i.e. by calculating the ratio of length to width $r = l/w$.

IVs of different pristine graphene samples measured in air and room temperature during the thesis are presented in figure 21 and the subscripts will differentiate between samples in different subfigures. These measurements were done by two-probe measurement geometry, which means that the junction resistance also includes the contact resistances. Figure 21a shows a set of three IVs measured with a close to identical device geometry ($r_a = 1.5$) with varying resistances. The differences can be explained by examining the graphene quality from SEM images at 21b. The lowest resistance ($R_{a1}(3.596 \pm 0.008)\,\mathrm{k\Omega}$ was observed in the device with the least darker areas that correspond to either folding or multilayered areas. The highest resistance ($R_{a2} = (4.140 \pm 0.013)\,\mathrm{k\Omega}$ was observed in the device with two clearly visible folds and large areas of multilayered graphene. The additional features visible in SEM images may have resulted increased scattering of charge carriers. However the additional differences in features may also have resulted in different contact resistances.

The IV of a similar device with different contact material and a longer channel ($r_c = 6.8 \pm 0.2 \approx 4.5 r_a$) is plotted in figure 21c with resistance $R_c = (34.49 \pm 0.02)\,\mathrm{k\Omega} \approx 8.33 R_{a2}$. The difference in the device resistivity is almost twice as high as the addition of the squares to the channel length. This can be attributed to the different contact resistances and the higher probability of grain boundaries, folds and multilayer domains present in a longer device. Figure 21d shows IVs of three devices made out of somewhat defected graphene with near identical geometry, where the randomness of the defects has caused differences in the resistances of the devices.

A four probe device seen in figure 22a was used to approximate the contact resistance of the nickel contacted devices to get an idea on the relative magnitude of contact and channel resistances in similar systems. Figure 22b shows the measured two-probe IVs between different terminals (Ti) and also the four-probe IV between the middle terminals ($T2 - T3$). The resistances determined from the IVs are listed in the table on the left in figure 23. These resistances were used to determine the contact resistance by two different methods: by directly comparing the two-probe and four-probe measurement of the terminals $T2 - T3$ and by transfer length method (TLM) using linear extrapolation of $R(l)$ function.

The two-probe resistance for the middle terminals was $R_{2p-T2T3} = (3.473 \pm 0.020)\,\mathrm{k\Omega}$ and the four-probe was $R_{4p-T2T3} = (462.2 \pm 2.1)\,\Omega$. The approximation of the contact

resistance R_{c-4-p} was done by subtraction as in equation (16):

$$R_{c-4-p} = R_{2p-T2T3} - R_{4p-T2T3} \pm \sqrt{(\delta R_{2p-T2T3})^2 + (\delta R_{4p-T2T3})^2}$$
$$= (3010.8 \pm 201.2)\,\Omega \approx (3.01 \pm 0.03)\ \mathrm{k}\Omega \quad (19)$$

Additionally the square sheet resistance was also calculated by first determining the number of squares between the terminals $T2$ and $T3$ $r_{T2T3} = 0.6174 \pm 0.0085$ and dividing the four-probe resistance with the number of squares to obtain $R_{\square-4-p} = (748.6 \pm 10.3)\,\Omega \approx (750 \pm 10)\,\Omega$.

The contact resistance was also calculated by making a linear fit to $R(l)$ function, ie. the two-probe resistances measured between different terminals as function of the graphene channel length. The $R(l)$ and the linear fit are plotted in figure 23 from which the contact resistance was determined as $R_{c-fit} = (3006 \pm 348)\,\Omega \approx (3.0 \pm 0.4)\,\mathrm{k}\Omega$. The slope of the fit was $(124.8 \pm 34.3)\,\Omega\,\mu\mathrm{m}^{-1} \approx (120 \pm 40)\,\Omega\,\mu\mathrm{m}^{-1}$ and was used to determine the square sheet resistance of graphene by multiplying it with the device width $(6.90 \pm 0.05)\,\mu\mathrm{m}$. The resulting square sheet resistance was $R_{\square-fit} = (861 \pm 237)\,\Omega \approx (900 \pm 300)\,\Omega$. The few data points and the differences in graphene between electrodes contributed to the large errors. Doping of the graphene by the metal of measurement electrodes and possible reflection caused by p-n junctions effect both of the measurements and add to the error in the measurement.

The single four-probe measurement cannot be used to determine resistivity for the nickel contacts or graphene channels with good accuracy but can be used to approximate the relative effects of different sources for the resistances of systems. The devices measured for figure 21a were made out of the same graphene sample and have the same contact material. The resistances of these devices were $(3.6 - 4.1\,\mathrm{k}\Omega)$. A similar range can be obtained by using the resistances measured earlier and taking the channel geometry ($r = 1.5$) into account: $\approx 3\,\mathrm{k}\Omega$ for the contacts and $1.5 \cdot 750\,\Omega \approx 1.1\,\mathrm{k}\Omega$ for the channels. This does not take into account the different width of the contacts, but the effect due to width of the contact should be less than due to other aspects of the geometry. These measurements do not also take into account the possibility of different fermi-levels in graphene. The measurements in next session were done to investigate the effects related to the doping of graphene by electric fields and extrinsic sources.

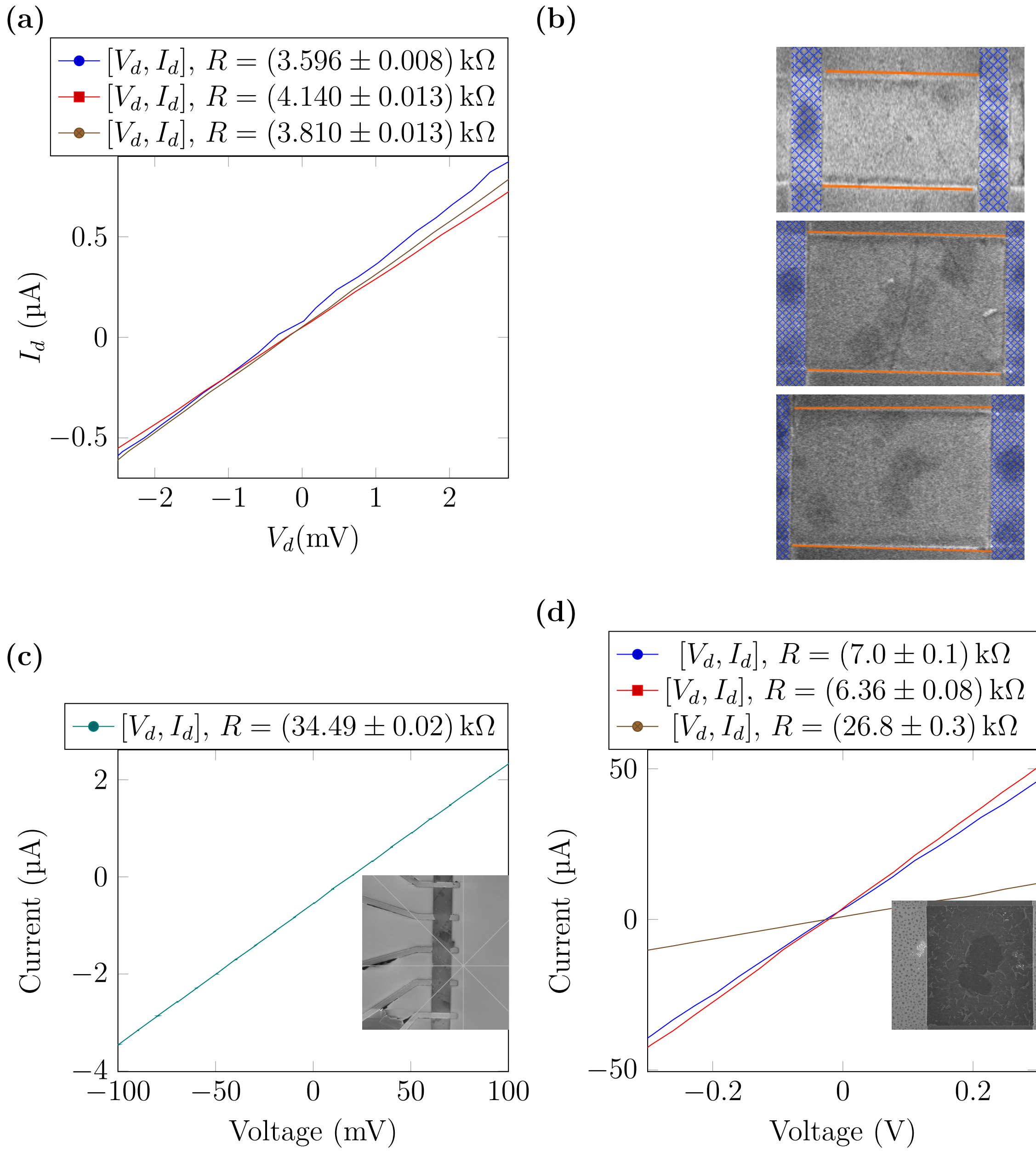

Figure 21. IV-measurements of two-probe devices with grounded gate. The device geometry is determined by width of the device (w), length of the device (l, width of the contact w_c and length of the contact l_c. The errors in the geometry are estimated from the ability to resolve the SEM-images.**(a)** The IVs of three different graphene devices with the same device geometry: $w = (4.7 \pm 0.1)$ µm and $l = (6.9 \pm 0.1)$ µm for the device channel and $w_c = (1.3 \pm 0.1)$ µm and $l_c = (4.7 \pm 0.1)$ µm for the contacts. The electrode material is nickel deposited on top of graphene. **(b)** The devices of a) in the same order as in the legend. The highest resistance was observed in device with two folds (middle one). The bottom one has damage near contact at left upper corner. The orange indicates the area of graphene and blue the contacts. **(c)** An IV of a grapehene device with geometry: $w = (4.5 \pm 0.1)$ µm and $l = (30.8 \pm 0.1)$ µm (only 2 working probes in the device) for the channel and $w_c = (1.3 \pm 0.1)$ µm and $l_c = (4.5 \pm 0.1)$ µm for the contacts. The electrode material is Ti/Pd 5 nm/25 nm of Pd on top of the graphene. **(d)** The IVs of three different defected graphene devices with similar defect density and the same device geometry: $w = (16.1 \pm 0.1)$ µm and $l = (14.3 \pm 0.1)$ µm for the device and $w_c = (16.1 \pm 0.1)$ µm and $l_c > 5$ µm. The electrodes are 25 nm nickel.

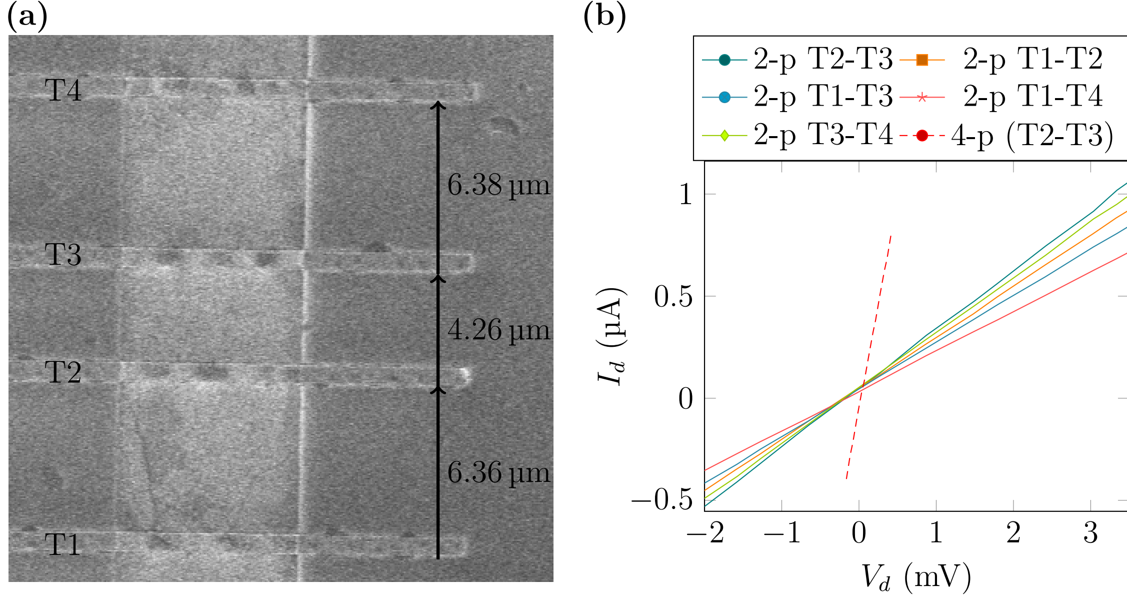

Figure 22. Four-probe IV-measurement of a grapehene device with nickel electrodes on top. **(a)** Scanning electron microscope image of a 4-probe device with metal contacts on top of the sample. The width of the device was (6.90 ± 0.05) µm. **(b)** IVs measured between different terminals of the four-probe device and the IV for the 4-probe measurement.

Terminal	Resistance (Ω)	Length (µm)
T1-T2	4010 ± 20	6.36 ± 0.05
T1-T3	4360 ± 20	10.62 ± 0.05
T1-T4	5130 ± 20	17.00 ± 0.05
T2-T3	3470 ± 20	4.26 ± 0.05
T2-T4	4270 ± 30	10.64 ± 0.05
T3-T4	3700 ± 20	6.38 ± 0.05
4-p	462 ± 3	-
4-p R_{c-4-p}	3010 ± 30	-
Fit R_{c-fit}	3000 ± 400	-
$R_{\square-4-p}$	750 ± 10	-
$R_{\square-fit}$	900 ± 300	-

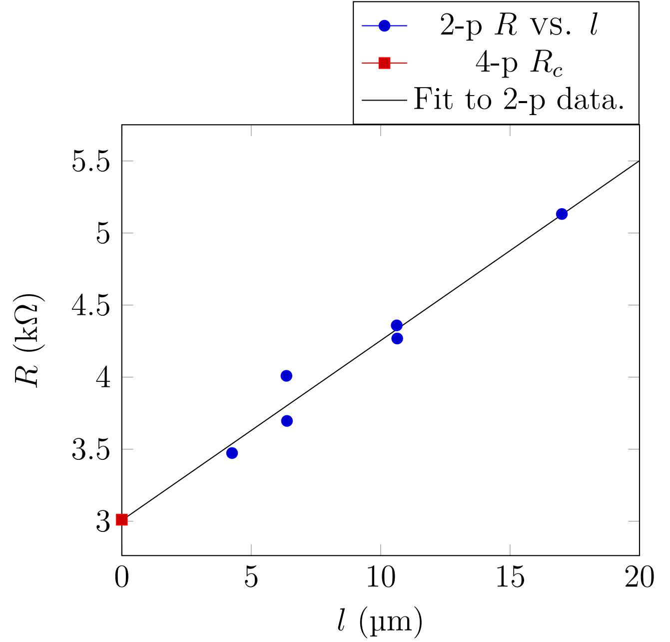

Figure 23. Resistances determined from the IV-curves between 2-p (two probe) between each terminal and 4-p (four probe) IV measurement in table and plotted. The contact resistance has been determined by linear fitting ($R = R_c + l\frac{R_\square}{w}$) to the data as R_c. The 4-p R_c is calculated from subtracting the 4-p resistance from the T2-T3 2-p measurement.

4.3 Back-gated measurements of pristine graphene

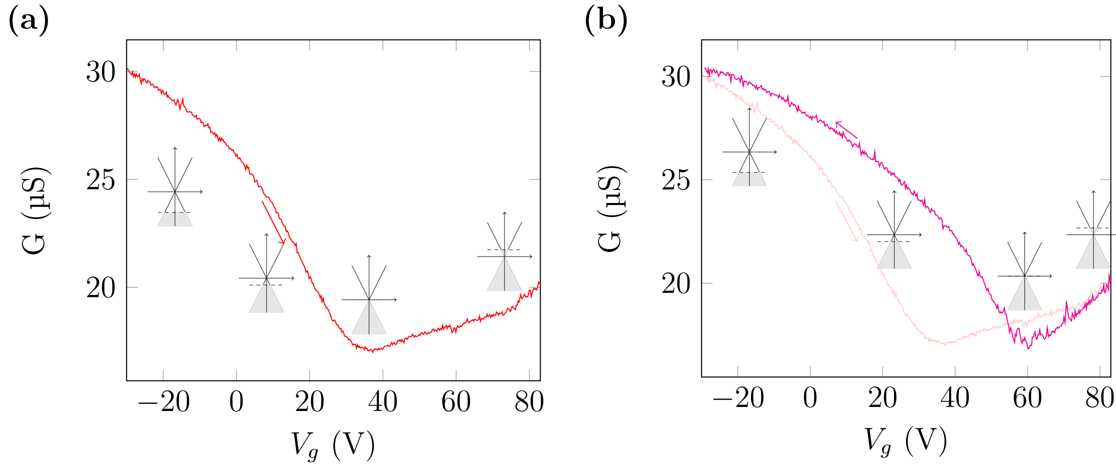

Figure 24. Two-probe gate sweep measurement of the transfer characteristics for the device in figure 21c. **(a)** Conductance of a graphene device vs. gate voltage swept from -35 V to 85 V. The dirac-point is shifted ≈ 35 V due to p-type doping. The n-type branch is not as steep due to charge traps and other sources of charge countering the gate charging. **(b)** The gate sweep from 85 V to -35 V following the measurement of (a) . The dirac-point is shifted by 60 V from the original position due to increased p-type doping caused by the gate voltage sweeps (reconfiguration of charge traps). The added noise in the vicinity of the dirac point might be related to unstable charge-traps and interaction with atmospheric particles.

The back-gated measurements in this section were done to probe the effect of applying a gate voltage (V_g) in the pristine graphene to see the form of $G(V_g(t))$. The interest of seeing the dirac point and the charge dynamics around the dirac point were among the main goals. The measurements of the hysteresis are comparable only if the $V_g(t)$ and the initial charging by charge traps was similar. This was taken into account on measurements where the hysteresis and transconductance were compared. The transfer characteristic curves were measured in ambient air, different humidities and at low temperatures.

A measurement of $G(V_g)$ for the device in figure 21c is plotted in figure 24. The measurement was done by applying first a voltage sweep from $V_g = -100$ V to $V_g = 100$ V and then back from 100 V to -100 V by using the same functional form with reverse signs. The drain current and drain-voltage were measured by two-probe geometry and the conductance was calculated and plotted in the figure.

Figure 24a shows visible dependency between G and V_g and a local minimum at 35 V, which corresponds to the charge carrier minimum of the device in the measurement environment. The figure shows an intuitive model for the average fermi-level for the graphene in the device. The device was highly p-type doped and the negative charging due to rising gate-voltage shifted the fermi-level up to and past the charge carrier minimum which was observed as conductance minimum. After passing the conductance minimum the majority charge carrier were electrons, but unlike predicted by relation (13) the steepness is clearly lower than in the p-type branch. The lesser steepness was likely caused by the charge-traps excited in the system that countered the charge added by gating and also by

additional particles absorbed on the device which withdrew electrons and resulted in a lower effective charging by gating. The shifted value for carrier minimum from 0 V to 35 V shows that the device was p-type prior to gating measurements. The returning scan in the figure 24b shows the (noisy) charge carrier minimum at 60 V and a steeper n-type slope than in the previous measurement. The steepness is related to different rate of excitation for charge carriers depending on the magnitude and direction of V_g sweep. The added noise is likely to be related to the unstability of the charge traps and the adsorbent dynamics.

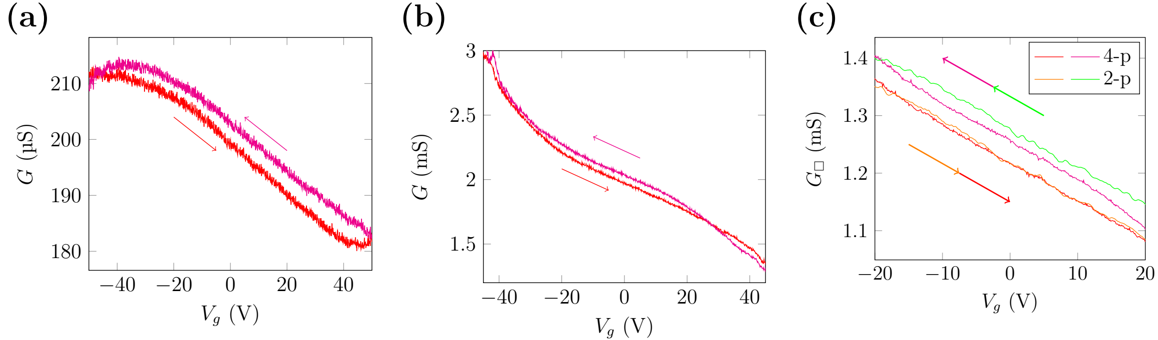

Figure 25. Four-probe measurement of transfer characteristic for pristine graphene devices. The curvature at high gate voltages are caused by leakage trough dielectric, which starts to rise rapidly at higher gating voltages. The square sheet conductances are calculated by scaling with the channel size and in case of two-probe measurement also subtracting the contact resistance determined in figure 23. **(a)** Two-probe measurement, $G = Id/V_{T1-T4}$. **(b)** Four-probe measurement, $G = Id/V_{T2-T3}$. **(c)** $G_\square(V_g)$ $(G \times l/w)$ from 2-p and 4-p measurements.

A measurement of the transfer characteristics done on a four-probe device is presented in figure 25. The measured device is same as in 22a with contact resistance of $R_c = 3\,\mathrm{k\Omega}$. The figures 25a and 25b show steep bending at high gating voltages due to leakage currents trough damaged dielectric from a few of the electrodes. The leakage was measured to be only 2 nA within $V_g = [-20, 20]$ ($I_d > 100\,\mathrm{nA}$), but rose rapidly after that which means that the results within range $V_g = [-20, 20]$ were still mainly determined by the graphene channel. The square sheet conductance $G_\square(V_g)$ was calculated from both results to figure 25c. In case of two-probe measurement I subtracted the $R_c = 3\,\mathrm{k\Omega}$ that was determined earlier for the device and scaled the conductance with number of squares in the channel $l/w = 2.46$. The four-probe measurement was just scaled with the number of squares in channel $l/w = 0.64$. The similarity of the results in figure 25c reassures that contact resistance can be approximated as constant with respect to electrostatic doping in the used range.

The hysteresis seen in the measurements is caused by the charged particles in atmosphere and by charge traps in dieletric. One prominent particle with a polar charge in air is H_2O and I measured the effects of the relative humidity on $G(V_g)$ and dI_d/dV_g at low humidity $\approx 30\,\%$ versus high $\approx 73\,\%$. The measurement was done by using the same $V_g(t)$ at all humidities to minimize the errors caused by charge trap excitation and was done first at low humidity (30 %) then at the high (73 %) and again at lower humidity (32 %) to reassure that no major changes happened to the device during measurements. The two-probe device was same as in the SEM image of figure 21d, with visible cracks and multilayered

domains. The measured transfer characteristics are presented in figure 26 along with the transconductance scaled with drain voltage $\frac{1}{V_d}\frac{dI_d}{dV_g} = \frac{g_m}{V_d}$ obtained with linear fits to the original data. The linear fitting was done for the data after filtering and smoothing. The hysteresis loop in $G(V_g)$ looks similar in all of the measurements, except that the conductance values in high humidity seem smaller. The g_m reveals that the slope of the high humidity measurement does not have same spike in the vicinity of the dirac-point as the low humidity measurements. Otherwise the $g_m(V_g)$s for all measurements seem to have followed a similar path. The reason for absence of spike can be explained by H_2O countering the charging and the effect of counter charging has higher impact on the G at low carrier concentrations. In basic terms: $g_m \propto dQ/dV_g = (\Delta Q_{gate} - \Delta Q_{H_2O})/\Delta V_g$, and the higher humidity will give rise to larger ΔQ_{H_2O}, which was the most visible at lower carrier concentrations.

A gate-scan of a two-probe device at low temperature, nearly 4.2 K, in low pressure helium is presented in figure 27. A linear fit for the range $Vg = 0 - 40\,\mathrm{V}$ gives slopes of $(-1.173 \pm 0.012)\,\mu\mathrm{S\,V^{-1}}$ and $(-0.570 \pm 0.007)\,\mu\mathrm{S\,V^{-1}}$ for the $G(V_g)$ at low temperature and at room temperature. The difference in slopes is due to higher mobility of charge carriers in graphene at lower temperatures. The higher range scan of $G(V_G)$ revealed the Dirac point at 84 V and the slopes before and after the the dirac point are closer to linear than at room temperature measurements. The hysteresis was also minimal in the low temperature graph. It seems that temperature may have played a part in the charge trap excitations along with the atmospheric effects.

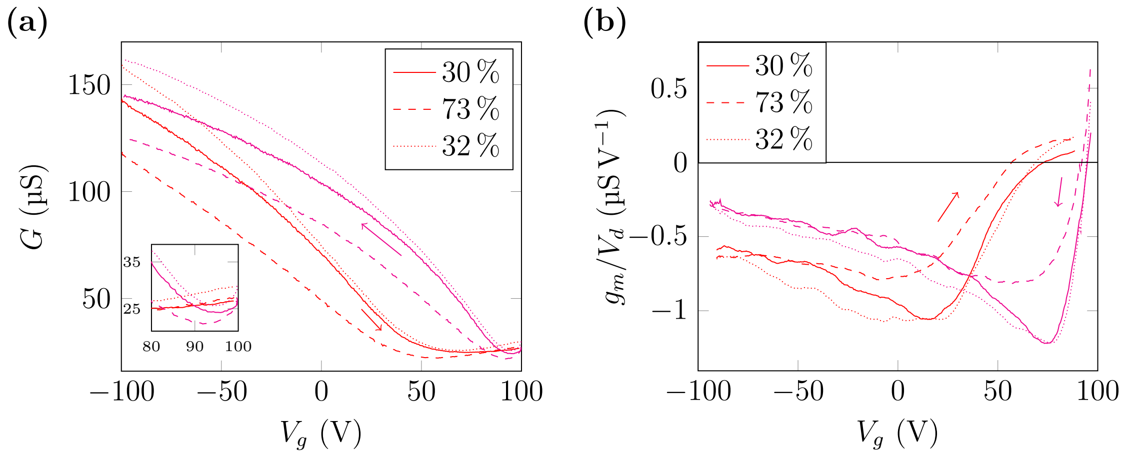

Figure 26. **(a)** The forward and backward gate sweeps for a device of partially cracked graphene. The sweeps were done first in a low humidity of 30 % then in a higher humidity of 73 % and then again in a low humidity of 32 %. **(b)** The g_m/V_d was calculated by smoothing and filtering the transfer characteristic graphs and using short range linear fits to get the slopes of the function. The differential graph shows that the counter charging by higher humidity in the vicinity of charge carrier minimum reduces the effective gating ie. the slope of conductance is less steep.

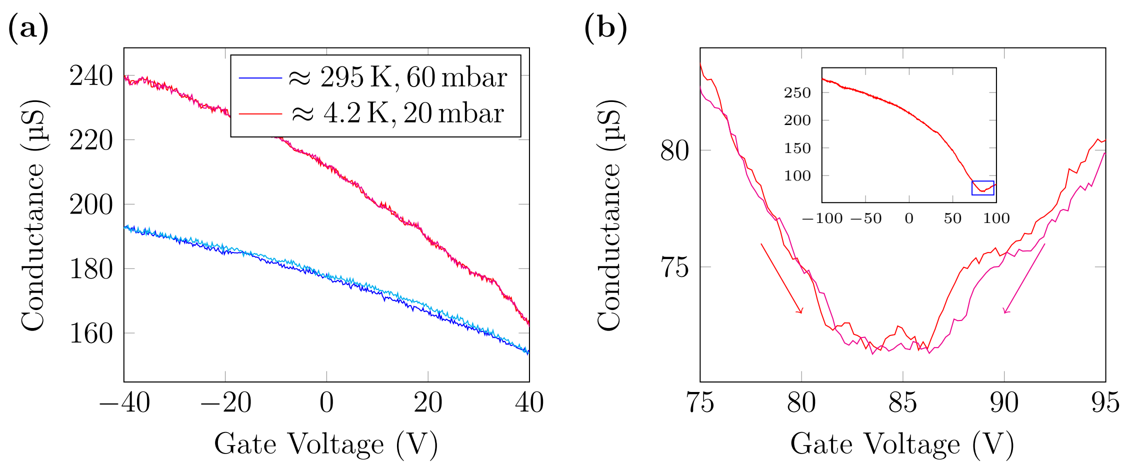

Figure 27. **(a)** -Measurement of transfer characteristics for two-probe contacted graphene device at room temperature and at nearly 4.2 K in helium atmosphere. **(b)** Larger gating range measurement in nearly 4.2 K (dipstick in liquid helium) and in helium atmosphere at the vicinity of the charge carrier minimum.

4.4 Oxidization of graphene by laser in ambient air

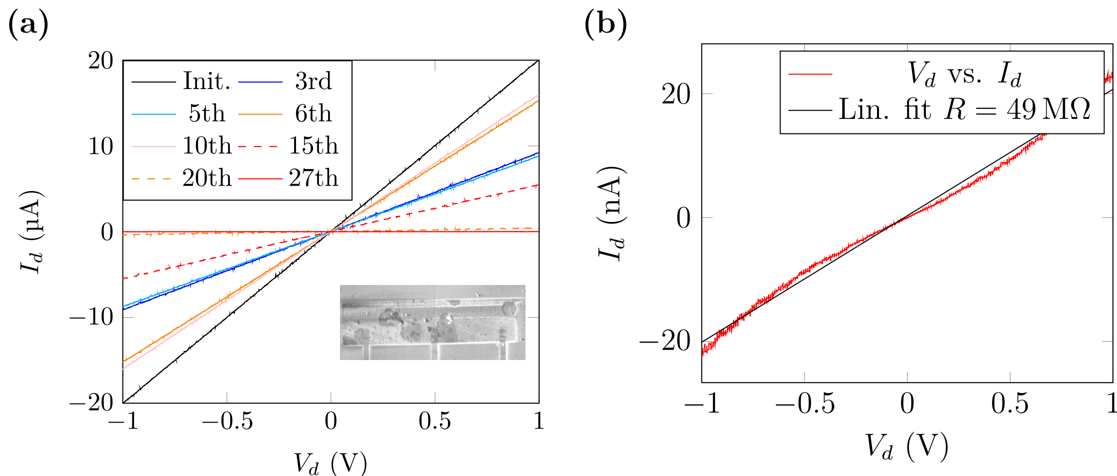

Figure 28. The resistance measurement of graphene during gradual femtosecond laser treatment testing. **(a)** A sampling of IVs measured during femtosecond laser treatment. 3rd and 5th were treated and measured under nitrogen purge and 6th, 10th, 15th, 20th and 27th were treated and measured in air. **(b)** The 25th IV-curve measured during oxidation and a linear fit to the data. The continued oxidization increased the resistance of the graphene device and the IV-response became less linear.

The treatment of the graphene by laser was done mainly by raster scanning with focused dot or in some cases by a single linear sweep. The power, the distance between scan points and the treatment times varied during the measurements. The FWM-signal was collected into maps in cases where the treatment was done for a uniform area instead of patterning certain types of features on the device. The initial testing of the femtosecond laser treatment was done in a gradual fashion by exposing the area of the sample completely with low power during a treatment step and measuring the IV in between the treatment steps. The chamber was purged with a dry N_2-flow to minimize the concentration of O_2, H_2O and CO_2 to avoid oxidization in the first five steps and after that the purge was turned off for the rest of the treatment cycles.

A sampling of a few IVs measured by two-probe geometry during the treatment cycle are shown in figure 28a. The response was linear until towards the end as seen in figure 28b. The gating of the sample was not responsive during measurements due to damage in the sample. The non-linearity may have also been the result of leakage in the system, but it is possible that the higher levels of oxidization caused additional charging effects or even semiconductor like properties.

Figure 29 shows the evolution of resistance of the graphene sample during the laser treatment cycle and a few of the four-wave-mixing images gathered during the treatment steps in air. The first treatment step in N_2 almost doubled the resistance of the device after which the rate for the rise of resistance was lower, switching from N_2-purge to measurement in air countered the changes in the resistance. The range in the measured resistances and the reversal of the process may mean that the device was just doped by the laser. The change of resistance during electrostatic doping in figure 24 is in the

same order of magnitude, where the device started as p-type doped and the charge carrier minimum moved towards the $V_g = 0$. The shift can be related to cleaning and reversing the p-type doping related to residual PMMA, but further measurements presented later in this section will show that also negative charge is added to the system by the femtosecond laser treatment in N_2. The treatment steps in air caused a rise of resistance in an exponential fashion with respect to treatment cycle number.

The intensity of the FWM-signal measured is related to features of the graphene in the area. A basic rule of thumb: a higher signal means thicker graphene. Four-wave-mixing images of the gradually oxidized graphene device are shown in figure 29, which shows that the graphene had multilayered domains on the single-layered device. The signal of single-layered graphene was reduced more in relative magnitude with respect to the multilayered domains which may have been due to of the fact that only the uppermost layer is in contact with air and oxidized whilst the lower layers were masked during the treatment.

Figure 30 shows a graphene sample, where an oxidation line has been drawn by using high power to form a fully insulating graphene device. The exposure of the line was done in parts to follow the evolution of device conductance during treatment. In the first exposure of the line a gap of 1 µm was left in middle. The gap was then closed by adding a laser point worth of exposure at the edges of the gap until the line was fully oxidized. The transfer characteristic curves show the electrical response of the device measured between the oxidation steps, but the measurement $G(V_g)$ of the device after closing the oxidation line is not shown as the currents were below the range of the instruments. The shapes of the transfer characteristic curves have additional features due to imaging done only at the oxidized area which results in uneven doping. This is discussed in the next section. The SEM-image in figure 30 shows that the oxidized structure blends well with the insulating substrate. The AFM-image shows that the oxidized area was still there as there were no clear edges and the height reading was only slightly modified. The results here would point out that the graphene can be modified to be fully oxidizing and the continuity of the layer seems to be preserved.

A simple way to test the masking effect of multiple layers in the oxidization process by a fold is illustrated in figure 31. The upper layer of the fold protects the graphene enclosed between the top layer and the substrate from contact with atmospheric particles. An experiment for a graphene device with a long fold between electrodes was done by oxidizing the graphene on and around the fold to limit the current transmission to mainly the graphene enclosed in the fold. A SEM image and transfer characteristics of the sample with the fold are shown in figure 32a and the FWM-image of the area is shown in figure 32b. The graphene was ablated before the measurement of the transfer characteristics to exclude the graphene not directly between the electrodes from the measurement. The transfer characteristics were measured in N_2 before imaging and showed a response which corresponds to a p-type doped graphene device.

A FFWM-mixing of the fold and transfer characteristics measured in air after the treatment are shown in figures 32c and 32d. The FWM-image shows a clear response from the folded area and fewer counts for the oxidized graphene. The gate-sweep corresponds to a p-type doped device with a small bump in the conductance curve. The small bump is related to the surrounding graphene which has been doped by the imaging and shifts the position in scan due to hysteresis in this area. The inset of the figure also shows the bump

earlier in the experiment, when the oxidation was not fully finalized.

The resolution limit of the oxidation is related to the size of the laser dot, but not at the diffraction limit. Figure 33a shows a single sweep oxidation line which was done over a small fold in graphene. The SEM-image in figure 33b shows that the area under the fold was not oxidized as in the earlier measurement. The width of the single sweep oxidation line is ≈ 150 nanometer and the area preserved under graphene is closer to 100 nanometer. The figure in 33c shows two lines of oxidization that were oxidized side by side in the processing to form a channel. However the contamination on the surface increased the scattering of laser and caused closing of the channel. Both of the images show that the graphene in the vicinity of the oxidation were also partially effected by the treatment.

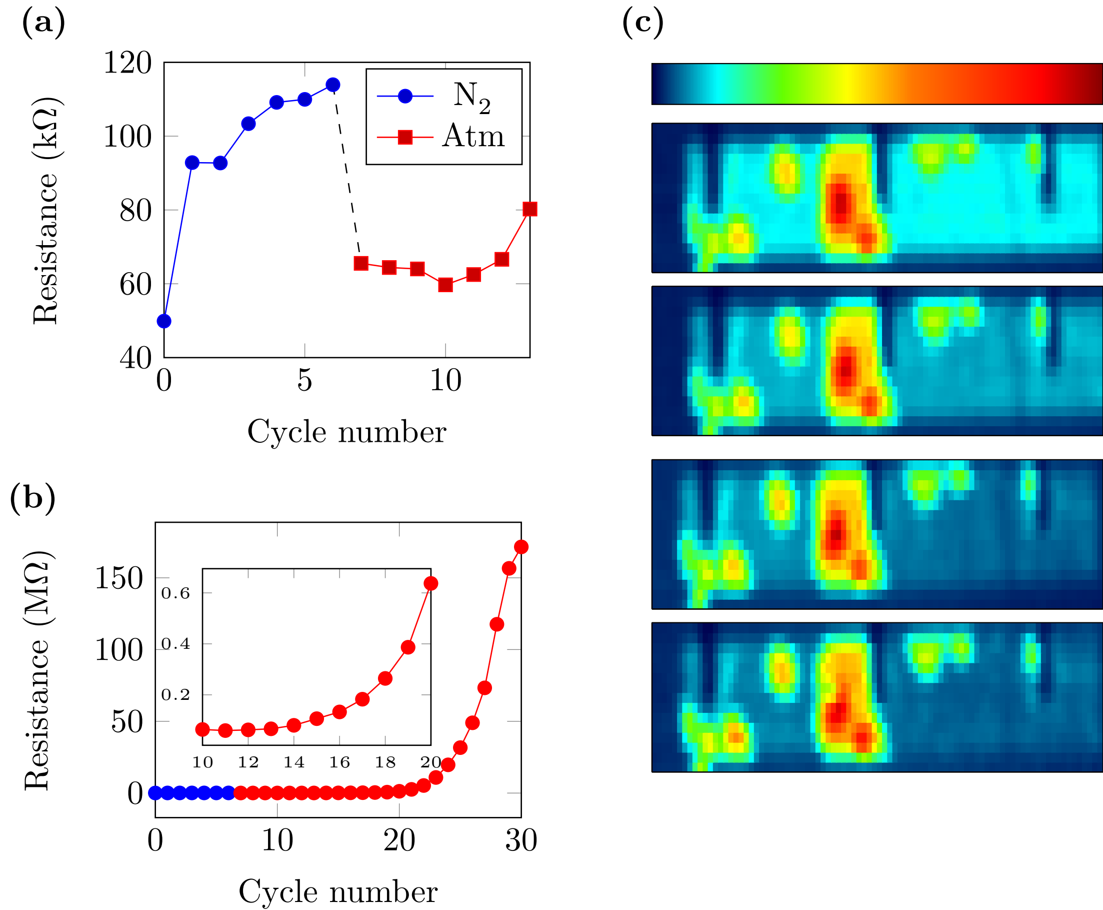

Figure 29. Successive gradual femtosecond laser treatment of graphene. **(a)** The resistance of the device during first treatment cycles done in N_2 and shift seen after switching the atmosphere. **(b)** The evolution of resistance during the whole treatment of the sample. Leakage in system trough substrate starts to effect the whole device resistance in the last steps. The inset shows the evolution of resistance during intermediate steps. **(c)** FWM-images taken during treatment) on the right for $Cycle = [10, 17, 23, 30]$, where signals are scaled to the highest counts (red) in each image. The low intensity lines (dark blue) on sample are caused by palladium electrodes under graphene. The higher intensity plateaus correspond to either thicker multilayered domains or folds. The intensity of single layered graphene (light blue in first image) is lowered during the treatment with respect to the signal of the thicker areas.

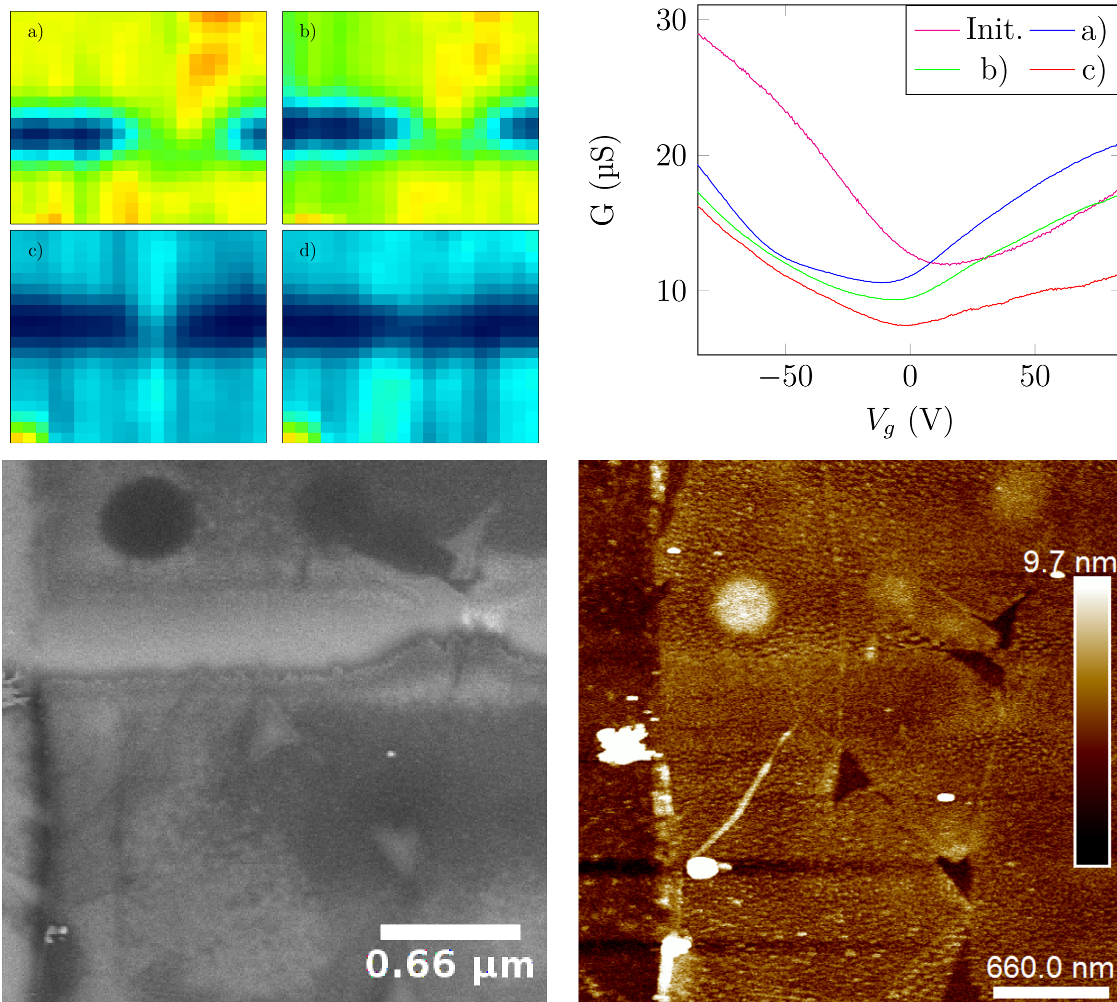

Figure 30. Creating an insulating gap in graphene (device of 21c) by oxidation. FWM-images (upper left) and G vs. V_g curves (upper right) measured before and between the oxidation steps a) a line of oxidation with initial gap of 1 µm, b) oxidizing an additional dot on both sides, c) adding a single dot of oxidation to right and finally d) oxidizing the graphene in the middle resulted in no current going trough the device. Imaging between oxidization was done in N_2 but only for a small part of the complete device, resulting in uneven doping. The SEM-image (lower left) and AFM image (lower right) were taken after closing the gap. The AFM-image seems to indicate that the continuity of the material has been preserved during oxidization.

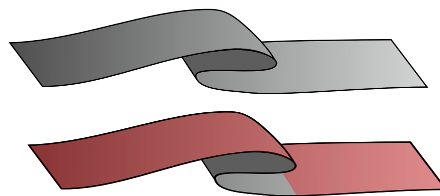

Figure 31. Illustrative drawing of the fold during graphene oxidization process, on top prior to oxidizing and on bottom after oxidizing (reddish for oxidized graphene). Only the upper layer of the graphene is exposed to the ambient atmosphere and shields the layers underneath.

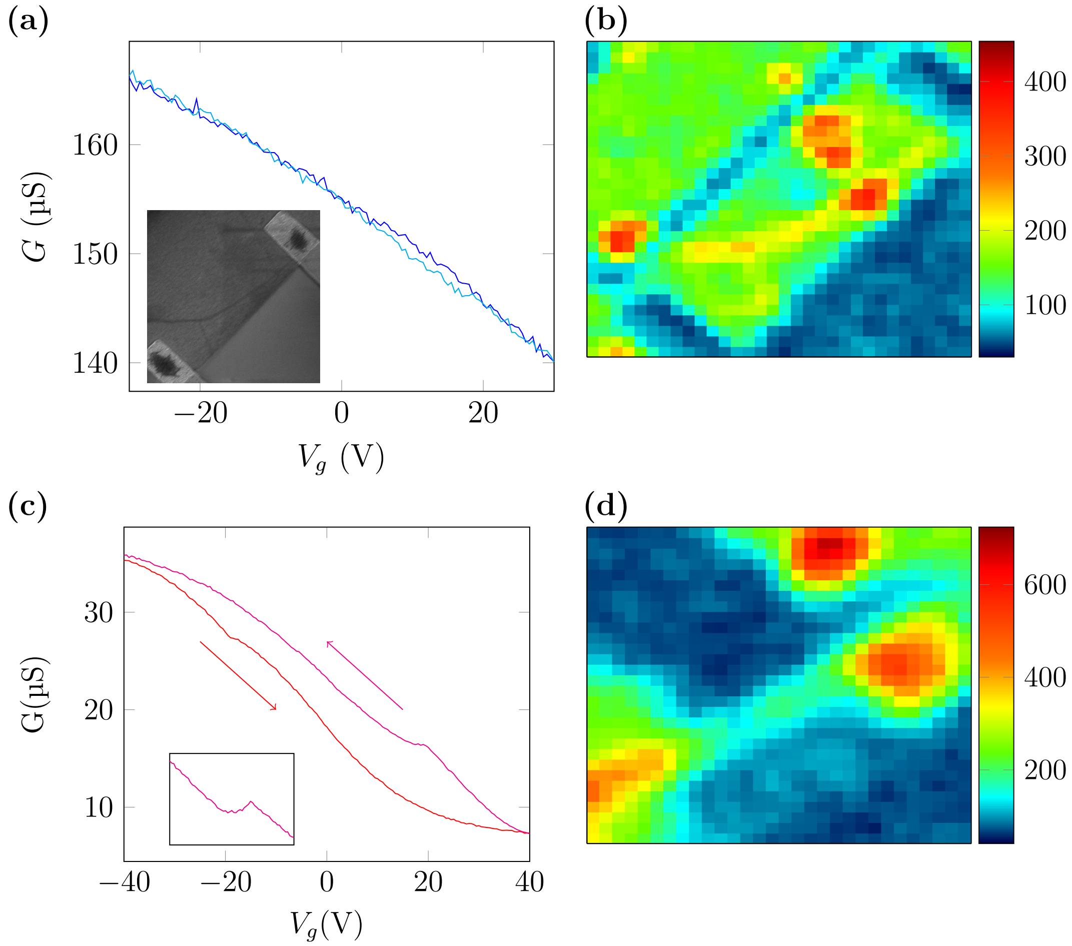

Figure 32. The fold oxidization experiment. The figures show the sample before and after oxidization (zoomed to the fold). The area between graphene was oxidized in such manner that the majority of the current was conducted by the fold. **(a)** The transfer characteristics were measured after using ablation to limit the boundaries of the device and before the imaging corresponds and shows that the device is p-type doped. The SEM image was taken prior to any laser treatment.**(b)** transfer characteristics and FWM-image of a graphene device taken after the measurement of transfer characteristics. The FWM-image shows a yellow linear feature which corresponds to a long multilayered area ie. folded graphene. **(c)** The measurement of transfer characteristics was done in air and the sharp bumbs are related to the charge carriers of the untreated graphene connected by the fold. The small subplot shows the form of ths bumb earlier in measurement, when the pattern was not fully oxidized. The $G(V_g)$ is that of p-type doped device with rapidly lowering density of states as function if gating. **(d)** FWM-signal shows still a response from the folded area after oxidization due to lower levels of graphene being masked by the fold.

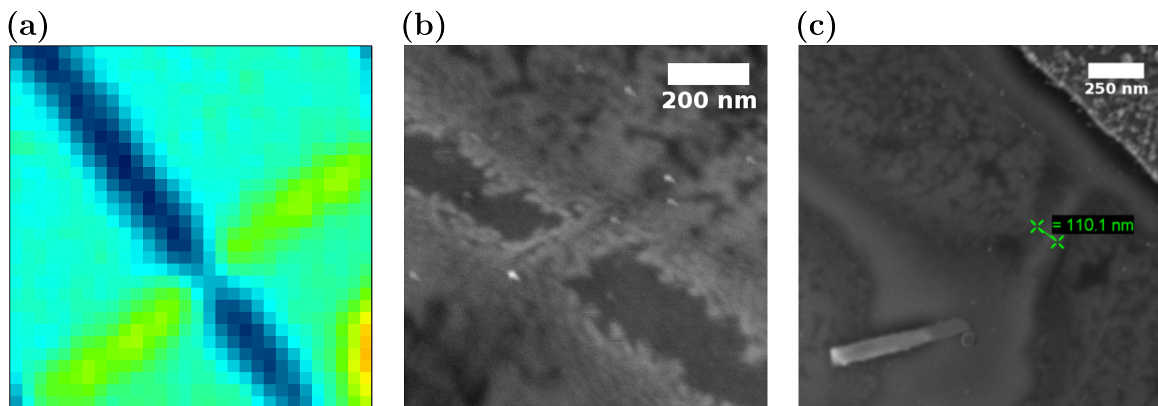

Figure 33. Resolution limits of femtosecond induced laser oxidation by free drawing. **(a)** FFWM-image of a single sweep oxidization line done over a small fold. **(b)** SEM-image at the intersection of the fold and the oxidization line. The transparent masking by folds or perhaps by other suitable materials might offer a way to go beyond the limitation in the resolution set by focusing a laser dot. **(c)** Single lines of oxidation close to each other can be easily connected if something on the surface increases the scattering. Here a defect has increased the scattering of laser and resulted in oxidization across a channel.

4.5 Doping of graphene by femtosecond laser in N_2

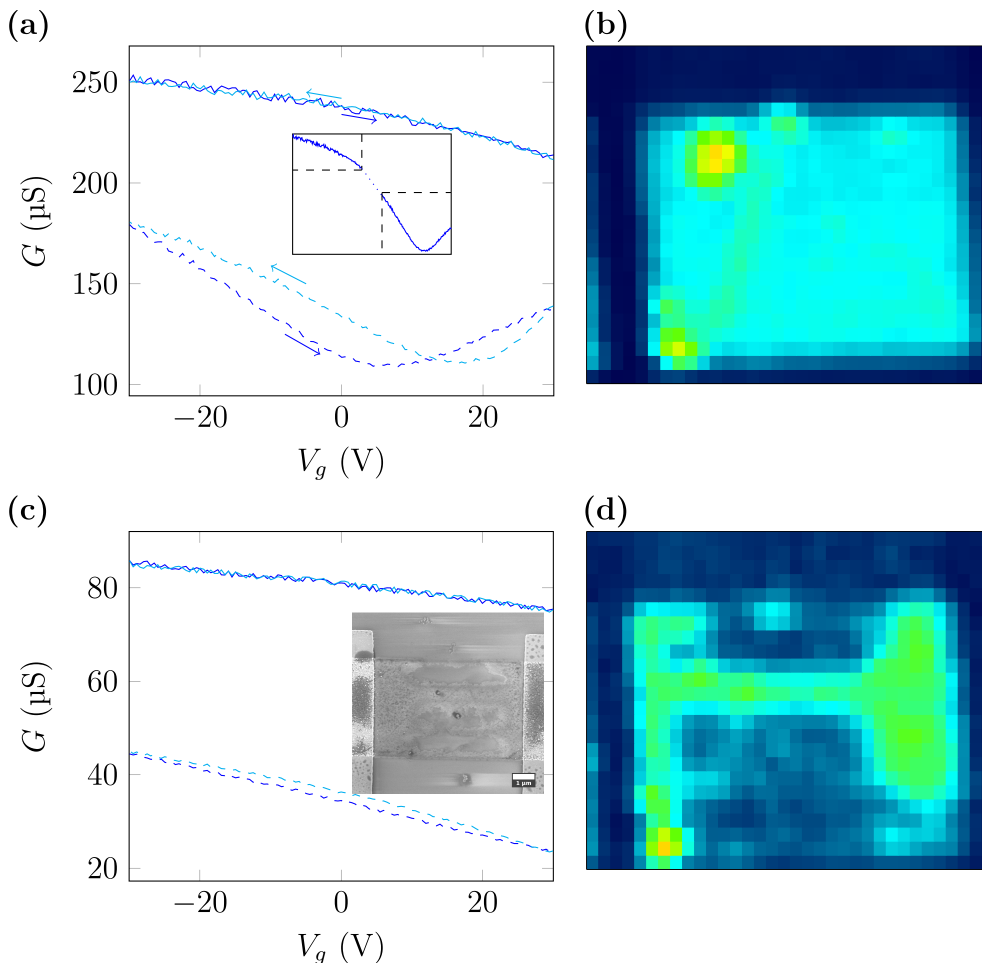

Figure 34. The effect of imaging on fermi-level of graphene under N_2-purge for pristine graphene device and same device with femtosecond laser oxidized channel. The step of laser was 250 nm for imaging. The electrical measurements were done under N_2-purging. **(a)** The gate voltage scan prior (solid) and after (dashed) FWM-imaging N_2. The device starts as highly p-type doped graphene with dirac-point out of scan range and ends up with fermi-level closer to the dirac-point after treatment imaging. The inset combines the pre- and post imaging (V_g shifted) curves to illustrate the initial configuration to get the similar function as in figures 24 and 26. **(b)** FWM-image taken during doping. **(c)** The gate sweeps after using laser oxidation to create a thinner channel (4.7 µm to 1.2 µm) in the graphene. The SEM-image shows that the oxidation was not completely uniform and which might have resulted in parallel conductors with the channel. The FWM-image was taken between the solid and dashed G vs V_g scans. The n-type doping was not strong enough to reveal the dirac point of the channel. **(c)** FWM-image of the partially oxidized sample.

Figure 34a shows gate-sweeps of a two-probe graphene device prior and after imaging, ie. femotsecond laser treatment in N_2. The initial transfer characteristics do not show a charge carrier minimum as the device seems to be highly p-type doped. However the $G(V_g)$ measured after the treatment in N_2 shows a clear local minimum and also increase of hysteresis. The hysteresis may have been the result of smaller charge carrier densities

having higher sensitivity to the effects of charge traps and was therefore largely absent in the initial highly p-type doped configuration. The two-conductance curves have also been fitted together (by eye) to form a continuous like transfer characteristics with similar form as in the earlier sweeps by a shift in V_g. The curve shows the intuitive model behind the laser doping, resulting in different initial charge on the sample and bringing in a different portion of the transfer characteristics. This effect corresponds to a different $V_{Ef}(n_0)$ in equation (17).

The same device was oxidized to form a thinner channel seen in the FWM-image and the SEM-image of figure 34b along with transfer characteristics before and after the imaging. The conductance drop between the initial and n-type doped sample is larger than earlier most likely due to smaller relative contribution from the contacts. The channel may have been partially oxidized during the treatment which might contribute to either p-type doping or smaller effective doping by the laser. It is also possible that the parallel partially oxidized channels for conductance have higher p-type doping and shift the charge carrier minimum of the sample.

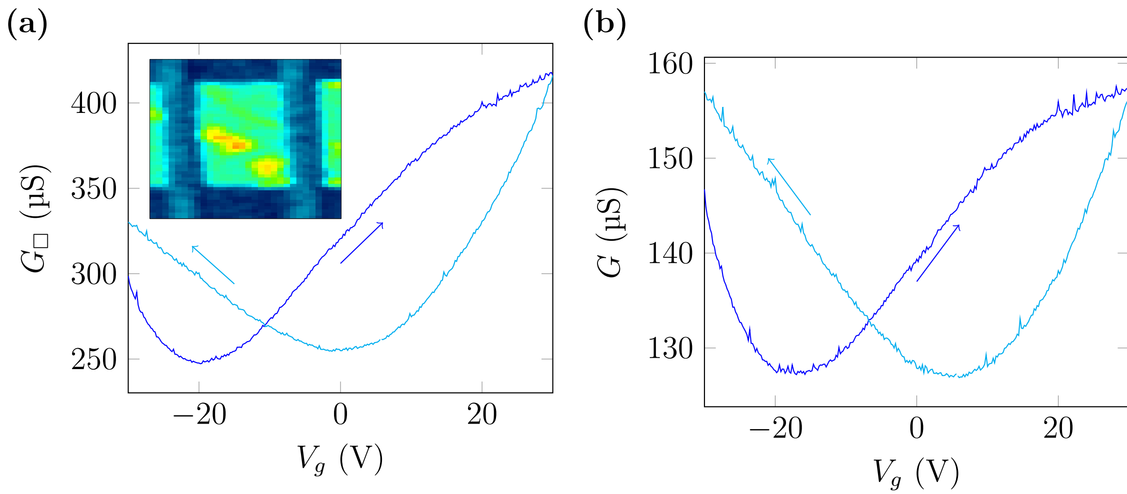

Figure 35. (a) A four probe $G_\square(V_g)$ for laser treated device with $l/w = 0.6$. The square sheet resistivity of the graphene is $3.83\,\mathrm{k\Omega} - 2.22\,\mathrm{k\Omega}$. The inset shows the FWM-image captured during the treatment. **(b)** the two-probe transfer characteristics measured between the source and drain electrode during the same measurement run. The measurement was done under N_2-purging.

A device with similar geometry as was measured for the transfer characteristics in figure 25 with four-probes was measured after imaging to uncover the effect of nitrogen doping on $G_\square(V_g)$. The measurement is presented in figure 35 along with the two-probe measurement done on the same run. The treatment was done only between and around the voltage probing electrodes in the middle of the device, which leaves parts of the device mostly untouched. The $G_\square$ was calculated by scaling the conductance calculated from the measured drain current and voltage with $l/w = 0.6$. The measurement shows that the lower limit on the square sheet conductance of graphene devices by doping was around $G_\square = 250\,\mathrm{\mu S}$. Compared to this result an untreated device with high p-type doping in figure 25 had $G_\square \approx 1\,\mathrm{mS}$. The hysteresis present in the measurement may have affected the magnitude of the minimum $G_\square = 250\,\mathrm{\mu S}$ along with uneven treatment profile which

would have created parallel conductors with different doping which may have resulted in a larger effective charge carrier minimum.

The location of the charge carrier minimum in the two-probe measurement was nearly the same as in the four-probe measurement. The treatment of the device left portions of the two-probe graphene device untouched and according to the prior measurement non-laser treated graphene is usually highly p-type doped. The high p-type doping results in lower response to gate and does not effect the location of the local conductance minimum caused by the charge carrier minimum of the treated area in the middle. Also it seems that the junctions (pn or np) between the differently doped areas did not effect the measurement in a clearly visible manner and the fact that the charge carrier minimum was observed for negative voltages suggests that the method is not limited to countering or removing positive charging but rather has added negative charging to the device.

The measurement of the transfer characteristics for laser doped devices have been done so far in an N_2-purged system which has been largely void of other atmospheric particles. A two-probe measurement of $G(V_G)$ for a laser doped device was done in both N_2 and in ambient air and the results are shown in figure 36 (same device as in figures 21c and 24). The initial $G(V_g)$ from $-100\,\mathrm{V}$ to $100\,\mathrm{V}$ in figure 36a shows a charge carrier minimum at $V_g = -50\,\mathrm{V}$ showing that the device was heavily n-type doped after the laser treatment. The scan in opposite direction has a bump and the effective charge carrier minimum corresponds to a higher conductance than the first sweep which may have been the result of higher hysteresis or instability of the charging for a small portion of the device.

The next measurement shown in figure 36b was done in ambient air with the same V_d and $V_g(t)$ applied to the device. The first sweep of the device had a charge carrier minimum at nearly the same location as earlier in N_2 but with a higher conductance. A part way into the n-branch the slope of the $G(V_g)$ went to zero which means that the gating did not add any charge carriers to the graphene channel. The scan to the opposite direction had the charge carrier minimum at +70 volts compared to -50 in the earlier loop. The form of the whole scan loop can be explained by high attraction and adhesion of charged molecules from the surrounding atmosphere to the laser doped graphene and the charging is not reversed instantly by switching the V_g-sweep direction. The measurement was followed by a similar sweep again in air for which the transfer characteristics are shown in figure 36c. The transfer characteristic had a similar form as earlier but the first conductance minimum had moved towards positive voltages which might mean that high gating was able to repel the positive charging received in the earlier loop, at least partially.

The transfer characteristic were measured again in N_2 after the measurements in air and the result is seen in the figure 36d. The transfer characteristic have a similar form to 36a but with a shifted charge carrier minimum and less steep branches. One can also see that the bump in the $G(V_g)$ in the $100\,\mathrm{V}$ to $-100\,\mathrm{V}$ scan was preserved from the earlier N_2 measurement, which means that the relative hysteresis or stability of the charging for the charge carrier densities of different areas was still present. This might mean that the effect causing n-type doping has not dissipated but rather charge was gathered on the sample which countered or screened the negative charging and shifted the charge-carrier minimum.

The laser treatment can also result in an uneven doping profile of the graphene devices which forms $p - p'$, $n' - n$ and $p - n$ junctions. The same device that was measured in the previous measurement was treated partially to get a clearly unevenly doped profile. The

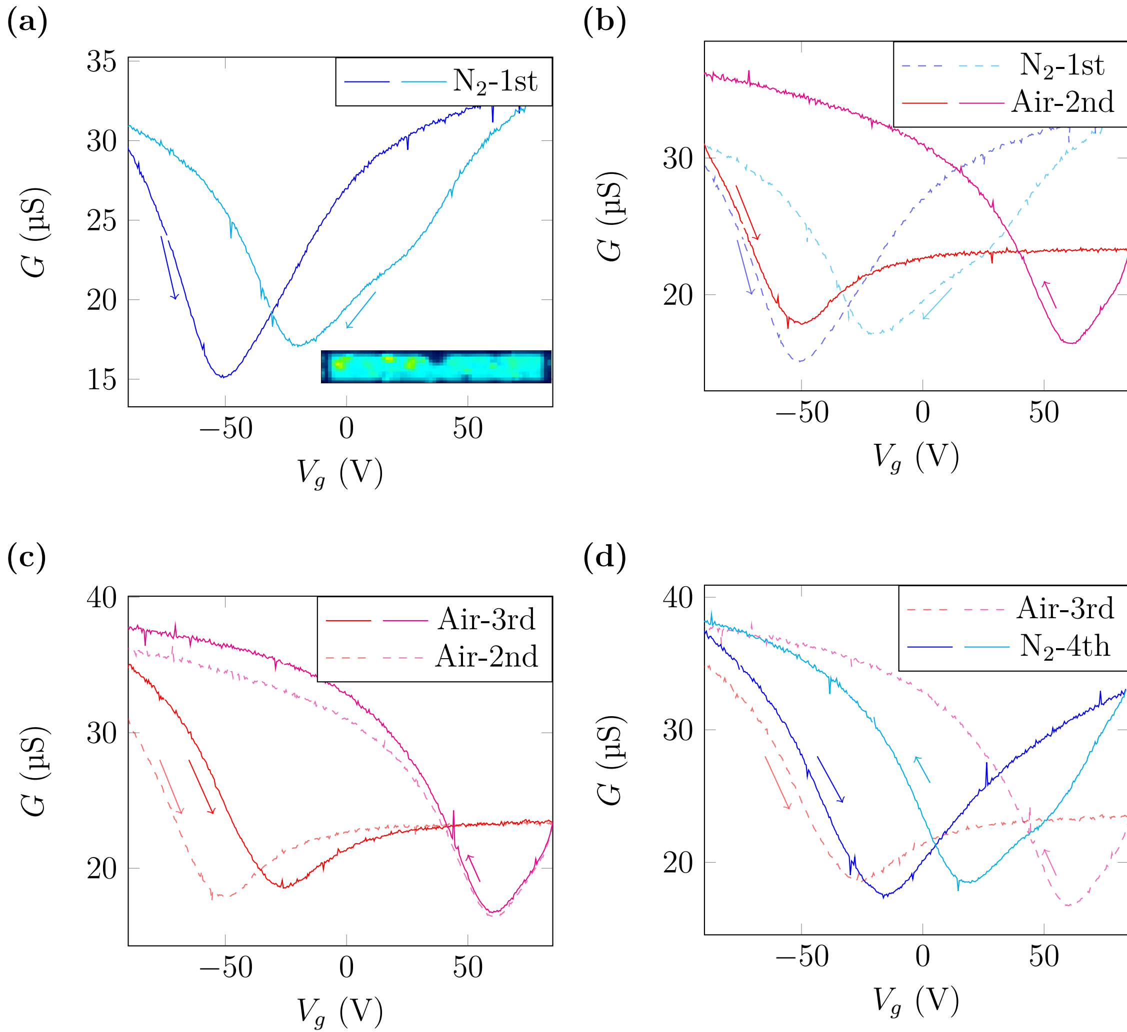

Figure 36. Stability and high hysteresis in femtosecond laser n-type doped device in N_2 and in ambient air. The measurements (from 1st to 4th) were done with same $V_g(t)$ following closely each other without additional treatment. The previous measurement is shadowed on background for comparison. **(a)** 1st gate sweep after n-type treatment on the sample, in N_2. The imaging was done in three portions that had a small overlap in total and the FWM-image is a reconstruction for the whole device. **(b)** 2nd gate sweep now in air. The $|\frac{dG}{dV_g}|$ flatlines after reaching the device reached a certain fermi-level on the n-branch, which results most likely from atmospheric particles (H_2O?) countering the charging. **(c)** The 3rd gate sweep, done in air, shows similar form as earlier, but with dirac-point of the first loop appearing at higher V_g value. **(d)** The fourth sweep, back to N_2, shows similar form as the first sweep, but with shifted dirac-point and more bent n-type branch.

treatment was done in N_2 with the same power for a length of 20 µm out of the total device length 31 µm. The gate sweep is shown in figure 37a along with the transconductance ($V_d^{-1}dG/dV_g$) by linear fitting in 37b. The initial gate sweep from -100 V to 100 V shows a conductance minimum at -80 volts and a clear flat plateau in the vicinity of -30 volts. The linear fitting resulted in a zero transconductance in the vicinity of the plateau. The returning sweep back from 100 V to -100 V appears to have a wide nearly constant

conductance minimum but a closer inspection showed two conductance minima and a local conductance maximum. The transconductance curve also shows three zeros, corresponding to the two conductance minima and one local maximum. The stark change in the shape of the curve for the returning sweep would point towards a higher instability in the charging of the newly treated area.

The formation of these transfer characteristic with more features ties tightly to conductors in series with different charge carrier minimums as written in equation (18). To illustrate the formation of these junctions I have smoothed the data from two previous $G(V_g)$-curves measured earlier from figures 36a and 36d and taken them as G_1 and G_2, which have been combined into a $G(V_g)$ of a single connected device in figure 37c. While combining each of the transfer characteristic curves were assumed to contribute half of the device length i.e. the resulting conductance is: $G = ((2G_1)^{-1} + (2G_2)^{-1})^{-1}$. The result shows similar features and magnitude for conductance minimum as the real measured curve and it seems that considering conductors in series is enough for diffusive channels of graphene with heterogeneous doping profiles. The transconductance calculated by linear fitting to this $G(V_g)$ is shown in figure 37d. Both the conductance and transconductance show similar features as the measured pn-junction.

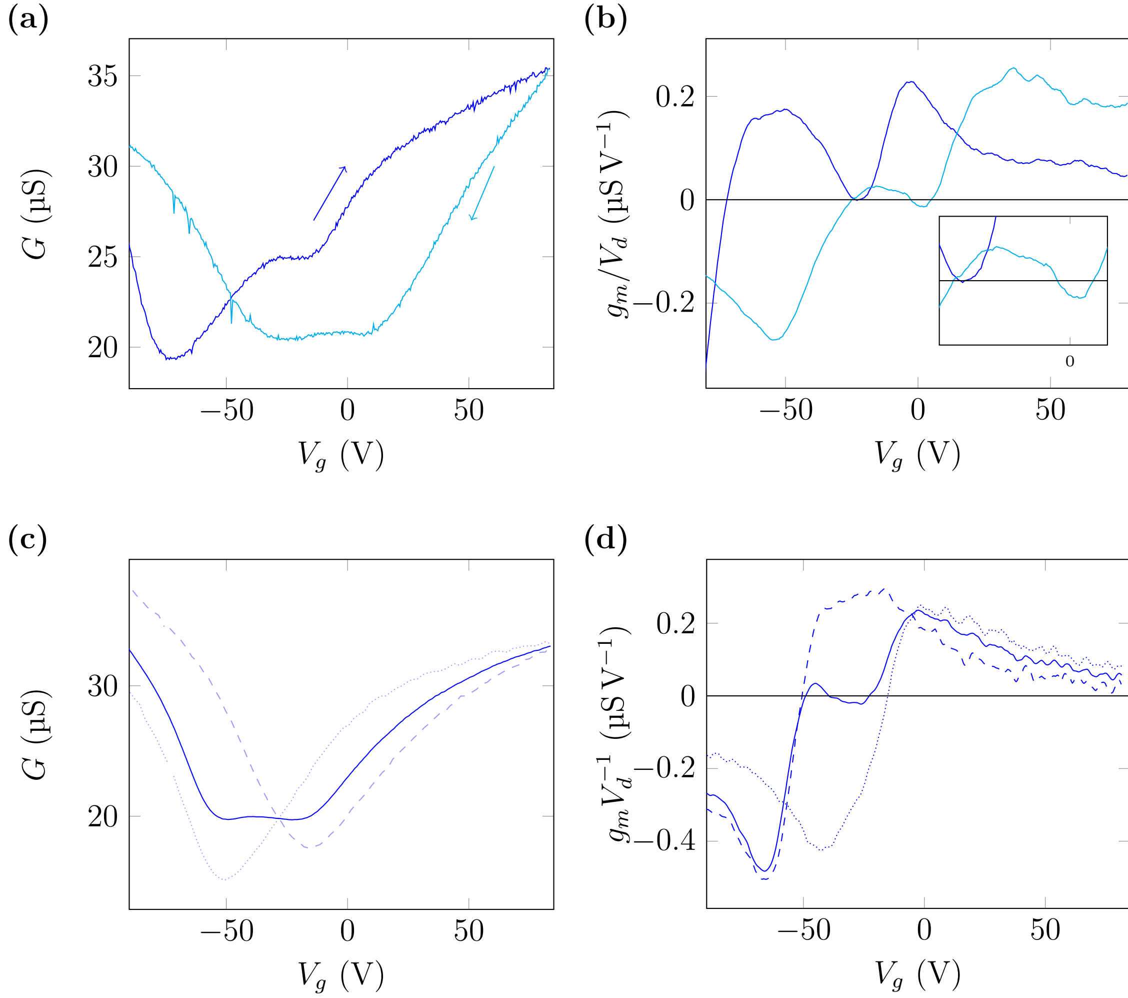

Figure 37. Unevenly doped graphene device and a calculation done by using two $G(V_g)$ with different doping levels. **(a)** An additional treatment done for the sample of 36 after the first measurement, but only for part of the device (20 µm of 31 µm), resulted in an additional flat plateau for first scan and two minima for the returning curve. **(b)** The transconductance g_m scaled by bias voltage V_d for traces in (a) obtained by linear fitting of the data. The light-blue curve shows three zeros corresponding to the two minima and one maximum for the $G(V_g)$ curve. The blue line shows two zeros for the conductance minimum and the flat plateau. **(c)** The $G(V_g)$ curves for range −100 V to 100 V from figure 36a and 36d used to model (or simulate) a pn-junction formation as two conductors in series. The solid curve is the result of these two conductors in series with each contributing half of the device. **(d)** The transconductance curves of 37c obtained by linear fitting to the measured and calculated data. The $g_m V_d^{-1}$ of the simulated $G(V_g)$ has similar features as the one obtained in (c) from the measured pn-junction.

5 Conclusions

The work done for this thesis helped in improving the synthesis of graphene, fabrication of electrode contacted devices and electrical measurements of graphene devices. The electrical measurements provided also additional information about the effects of femtosecond laser treatment on the electrical properties of graphene devices.

The work on the synthesis focused on solving some of the common problems faced in the CVD production of graphene with the synthesis setup at University of Jyväskylä. The quality and durability of the catalytic copper surfaces during the synthesis is important in producing continuous graphene. The work in this thesis identified that using a metallic thermocouple (fig. 11a) in the system during the steps of synthesis contributes largely to the appearance of the dewetting points (fig. 14c) which can be countered by using quartz based loading rod (fig. 11b). The dewetting might be due to the high temperatures used in the synthesis resulting in deposition of the metal of the thermocouple on the surface or metallic rod can collect depositions during the synthesis by decomposing carbon and later the depositions might be relocated on to the catalytic surface. The samples fabricated by bubbling of carrier gas trough liquid ethanol resulted often in formations of amorphous carbon on the samples (fig. 16c) and not so well repeatable results in the synthesis process. Switching of the carbon source to gaseous methane resulted in more repeatable result and no amorphous carbon was seen on the surfaces after the change. However the flow range of pure methane provided by the MFCs of the system were too high to produce single-layered graphene. This could be improved by switching to a diluted methane gas or to a mass flow controller suitable for lower flows, or possibly by using shorter growth times, but it might be preferential to have longer growth times to obtain larger domains [13].

Fabrication of the graphene devices require additional steps of lithography and the added treatments in resist can cause additional damage. The method developed in this thesis relies on using a copper layer between the resist and the graphene, and metal masks during etching (fig. 12). The method proved to be able to produce electrode contacted graphene and the SEM imaging (fig. 20a) did now show additional resist on the samples after the processing. However the success of process is still dependant on a soft-lift off process due to low adhesion of graphene on the substrate and metals to graphene, and the Raman characterisation (fig: 20b) show high D-bands after the fabrication. Further development of the graphene-resist contact free device fabrication method requires focus on making the lift-off softer and finding the reason for the higher D-band, which could also be related to the synthesis.

The electrical measurements of pristine graphene devices measured the effects of contact resistance in the systems, the conductance dependency of CVD-graphene on gate voltage and showed some of the related effects in the response. The resistance measurements of different graphene devices (fig. 21) shows that the device resistance depends on the geometry and quality of the graphene channels. The gated measurements of the pristine graphene samples showed that the initial configuration of the devices after fabrication is p-type doped and the gate-response was affected by humidity and charge traps but the dynamicity of the gate resistance is not significant (fig. 25c). The low temperature measurement (fig. 27) showed that it is possible to reach the linear relation in the vicinity of the dirac-point and the temperature and ambient gases may cause less linear $G(V_g)$ relation in the measurement. The shift of the dirac point from

$V_g = 0\,\mathrm{V}$ can be related to doping of graphene by the substrate or by adsorbates such as hydrocarbons [52, 53].

The electrical measurements on the two-photon oxidized graphene showed that the resistivity of graphene can be continuously tuned upwards locally by femtosecond laser pulsed treatment as shown in figure 29 and the patterning turns graphene into complete insulating material but the continuity of the atomic layer seems to be preserved (fig. 30). This means that it is possible to draw conducting paths on a single layer of graphene, but still preserve the structural integrity at least partially. It would be worth to further study if the interface of the oxidized graphene and graphene is more stable than that of milled or etched graphene devices. The insulating state is likely the result of the conducting π-electrons being removed from the lattice due to bonding of the oxidation groups, the majority of which are hydroxyl groups (OH) [54]. The oxidation also seems to have affected only the top layer of folded graphene with local multilayered structure and the the features sandwiched between the substrate and the top layer are still conductive as was seen in figure 32a.

The oxidation is formed by small islands of oxidations growing larger until fully covering the surface which seems to mean that the edge of oxidized graphene is more reactive in the processing [55]. The oxidation line done over the fold in figure 33a shows that the whilst the inner part of the lines seems to be completely insulating the area around is also partially affected. The dose of the laser is lower at the edge of the line as the treatment was done in a single sweep and the oxidization islands at the areas with lower dose have not made the material completely insulating, however this effect would still modify the quality of conductive channels drawn by line oxidization. The elevated vulnerability to oxidation by laser at the vicinity of the oxidized features may have been partially responsible for connecting the two different lines of oxidation in figure 33b. The increased reactivity in the vicinity of oxidized features might limit the resolution of graphene channels that can be done by using mask free laser drawing. However the result in figure 32 shows that one can use graphene folds to prevent the oxidization and this method is analogous to using transparent masking which protects the graphene from coming in contact with atmospheric particles. The usage of masking in two-photon oxidization might allow creation of narrow graphene devices, which perhaps could be even suspended.

The femtosecond-laser treatment of graphene in N_2 resulted in n-type shifted doping of devices, as is shown in figure 34a. The oxidization measurements showed that the graphene can be functionalized by the laser, where the absence of other reactants under N_2-purge might result in formation of defects rather than oxidization. The added defects or stress caused by these defects may have acted as negative charge centers in the system. Defected graphene might be also more susceptible to addition of chemical groups in air, charge traps and adsorption of molecules. The evolution of doping profile experienced in figure 36 suggests that the atmospheric gasses effect the doping highly at n-branch, which might be the result of the elevated susceptibility to adsorbates. The moving of the dirac point to the right between figures 36a and 36d might be the result of defects having a higher negative charge during the gate voltage sweeping and interacting strongly with the charge traps in SiO_2 during the measurement, resulting in partially withdrawn doping from the system. The electric field induced during the measurement may not have been strong enough to counter this interaction. However this is still speculation on the possible mechanism and additional investigation would be required to confirm the

proposed defect induced doping mechanism. The n-type doping by laser was also used to pattern a graphene pn-junction with two charge carrier minimums (fig. 37a) and the response of this kind of junction was also simulated by calculating the conductance of two differently doped areas in series (fig. 37c). Doping patterns have previously been drawn by creating defect induced charging in boron-nitride in contact with graphene,resulting in addition of charge carriers at the treated regions [56].

The femtosecond laser induced oxidization and n-type doping both show promise in fabrication of graphene based electronics. The gradual modification of the properties of graphene surfaces might be valuable for example in sensor applications, where increased sensitivity of electrical properties to environment might result in extremely sensitive sensors. Additionally the oxidization of graphene combined with high resolution masking might provide a way to make more stable graphene nanoribbons. Both of the methods are likely to function in suspended devices which might make them useful in fabrication of resonators or in investigation of exotic charge carrier properties of graphene.

References

[1] K. S. Novoselov et al. Electric field effect in atomically thin carbon films. *Science*, **306**:666–669, 2004.

[2] K.S. Novoselov et al. Two-dimensional atomic crystals. *PNAS*, **102**:10451–10453, 2005.

[3] A. K. Geim and I. V. Grigorieva. Van der waals heterostructures. *Nature*, **499**:419–425, 2013.

[4] C. Lee et al. Measurement of the elastic properties and intrinsic strength of monolayer graphene. *Science*, **321**:385–388, 2008.

[5] J-H Chen et al. Intrinsic and extrinsic performance limits of graphene devices on SiO_2. *Nature Nanotechnology*, **3**, 2008.

[6] K. S. Novoselov et al. Two-dimensional gas of massless dirac fermions in graphene. *Nature*, **438**:197–200, 2005.

[7] M. I. Katsnelson et al. Chiral tunneling and klein paradox in graphene. *Nature Physics*, **2**:620 – 625, 2006.

[8] S. Chen et al. Electron optics with p-n junctions in ballistic graphene. *Science*, **30**:1522–1525, 2016.

[9] N. Levy et al. Strain-induced pseudo–magnetic fields greater than 300 tesla in graphene nanobubbles. *Science*, **329**:544–547, 2010.

[10] G. Ko et al. Graphene-based nitrogen dioxide gas sensors. *Current Applied Physics*, **10**:1002–1004, 2014.

[11] G. Lu et al. Gas detection using low-temperature reduced graphene oxide sheets. *Appl. Phys. Lett.*, **12**:083111, 2009.

[12] Y. Hernandez et al. High-yield production of graphene by liquid-phase exfoliation of graphite. *Nature Nanotechnology*, **3**:563–568, 2008.

[13] X. Wu et al. Growth of continuous monolayer graphene with millimeter-sized domains using industrially safe conditions. *Scientific Reports*, **6**:21152, 2016.

[14] Z. Yan et al. Toward the synthesis of wafer-scale single-crystal graphene on copper foils. *ACS Nano*, **6**:9110–9117, 2012.

[15] Q. Yu et al. Control and characterization of individual grains and grain boundaries in graphene grown by chemical vapour deposition. *Nature Materials*, **10**:443–449, 2011.

[16] J. Aumanen et al. Patterning and tuning of electrical and optical properties of graphene by laser induced two-photon oxidation. *Nanoscale*, **7**:2851–2855, 2015.

[17] A. H. C. Neto et al. The electronic properties of graphene. *Reviews Of Modern Physics*, **81**:109–162, 2009.

[18] P. R. Wallace. The band theory of graphite. *Phys. Rev.*, **71**:622–634, 1947.

[19] E. McCann et al. The low energy electronic band structure of bilayer graphene. *Eur. Phys. J. Spec. Top.*, **148**:91–103, 2007.

[20] S. Latil and L. Henrard. Charge carriers in few-layer graphene. *Phys. Rev. Lett.*, **97**:036803, 2006.

[21] T. Stauber et al. Electronic transport in graphene: A semi-classical approach including midgap states. *Physical Review B*, **76**:205423, 2007.

[22] N. M. R. Peres et al. Electronic properties of disordered two-dimensional carbon. *Physical Review B*, **73**:125411, 2006.

[23] S. Dröscher et al. Quantum capacitance and density of states of graphene. *Appl. Phys. Lett.*, **96**:014009, 2010.

[24] F. Xia et al. The origins and limits of metal-graphene junction resistance + suppl. online material. *Nature Nanotechnology*, **6**:179–184, 2011.

[25] G. Giovannetti et al. Doping graphene with metal contacts. *Phys. Rev. Lett.*, **101**:026803, 2008.

[26] K. Nagashio and A. Toriumi. Density-of-states limited contact resistance in graphene field-effect transistors. *Japanese Journal of Applied Physics*, **50**:070108, 2011.

[27] V. V. Cheianov and V. I. Falko. Selective transmission of dirac electrons and ballistic magnetoresistance of n-p junctions in graphene. *Phys. Rev. B*, **74**:041403, 2006.

[28] P. Joshi et al. Intrinsic doping and gate hysteresis in graphene field effect devices fabricated on SiO_2 substrates. *J. Phys. Condens. Matter*, **22**:334214, 2010.

[29] V. E. Dorgan et al. Mobility and saturation velocity in graphene on SiO_2. *Appl. Phys. Lett.*, **97**:082112, 2010.

[30] H-Y Chiu et al. Controllable p-n junction formation in monolayer graphene using electrostatic substrate engineering. *Nano Lett*, **10**:4634–4639, 2010.

[31] X. Li et al. Large-area synthesis of high-quality and uniform graphene films on copper foils. *Science*, **324**:1312–1314, 2009.

[32] A. Guermouneo et al. Chemical vapor deposition synthesis of graphene on copper with methanol, ethanol, and propanol precursors. *Carbon*, **49**:4204–4210, 2011.

[33] Z. Sun et al. Growth of graphene from solid carbon sources. *Nature*, **549**:549–552, 2010.

[34] K. M. Reddy et al. High quality, transferrable graphene grown on single crystal cu(111) thin films on basal-plane sapphire. *Appl. Phys. Lett.*, **98**:113117, 2011.

[35] I. Vlassiouk et al. Role of hydrogen in chemical vapor deposition growth of large single-crystal graphene. *ACS Nano*, **5**:6069–6076, 2011.

[36] X. Li et al. Evolution of graphene growth on ni and cu by carbon isotope labeling. *Nano Lett.*, **9**:4268–4272, 2009.

[37] H. Wang et al. Controllable synthesis of submillimeter single-crystal monolayer graphene domains on copper foils by suppressing nucleation. *J. Am. Chem. Soc.*, **134**:3627–3630, 2012.

[38] D. H. Jung et al. Surface diffusion directed growth of anisotropic graphene domains on different copper lattices. *Scientific Reports*, **6**:21136, 2016.

[39] R. He et al. Large physisorption strain in chemical vapor deposition of graphene on copper substrates. *Nano Lett.*, **12**:2408–2413, 2012.

[40] D. L. Miller et al. Giant seondary grain growth in cu films on sapphire. *AIP Advances*, **3**:082105, 2013.

[41] J. W. Suk et al. Transfer of cvd-grown monolayer graphene onto arbitrary substrates. *ACS Nano*, **5**:6916–6924, 2011.

[42] J. Chan et al. Reducing extrinsic performance- limiting factors in graphene grown by chemical vapor deposition. *ASC Nano*, **6**:3224–3229, 2012.

[43] J. Lee et al. Clean transfer of graphene and its effect on contact resistance. *Appl. Phys. Lett.*, **103**:103104, 2013.

[44] J. D. Wood et al. Annealing free, clean graphene transfer using alternative polymer scaffolds. *Nanotechnology*, **26**:055302, 2015.

[45] Z. Cheng et al. Toward intrinsic graphene surfaces: A systematic study on thermal annealing and wet-chemical treatment of SiO_2-supported graphene devices. *Nano Lett.*, **11**:767–771, 2011.

[46] Y-C Lin et al. Graphene annealing: How clean can it be? *Nano Lett.*, **12**, 2012.

[47] M. C. Lemme et al. Etching of graphene devices with a helium ion beam. *ACS nano*, **3**:2674–2676, 2009.

[48] H. Al-Mumen et al. Singular sheet etching of graphene with oxygen plasma. *Nano-Micro Lett.*, **6**:116–124, 2014.

[49] S. Kumar et al. Reliable processing of graphene using metal etchmasks. *Nanoscale Research Letters*, **6**:390, 2011.

[50] Graphenea Inc. Monolayer graphene on sio2/si. `https://www.graphenea.com/collections/buy-graphene-films/products/monolayer-graphene-si02-pack-4u`. Accessed: 2017-02-26.

[51] S. Das et al. Measurements of the adhesion energy of graphene to metallic substrates. *Carbon*, **59**:121–129, 2013.

[52] S. Goniszewski et al. Correlation of p-doping in cvd graphene with substrate surface charges. *Scientific Reports*, **6**:22858, 2016.

[53] Z. Li et al. Effect of airborne contaminants on the wettability of supported graphene and graphite. *Nature Materials*, **12**:925–931, 2013.

[54] A. Johansson et al. Chemical composition of two-photon oxidized graphene. *Carbon*, **115**:77–82, 2017.

[55] J. Koivistoinen et al. From seeds to islands: Growth of oxidized graphene by two-photon oxidation. *J. Phys. Chem. C,*, **120**:22330–22341, 2016.

[56] L. Ju et al. Photoinduced doping in heterostructures of graphene and boron nitride. *Nature Nanotechnology*, **9**:348–352, 2014.

[57] J. Aumanen et al. Supplementary online information: Patterning and tuning of electrical and optical properties of graphene by laser induced two-photon oxidation. `http://www.rsc.org/suppdata/nr/c4/c4nr05207b/c4nr05207b1.pdf`, 2014.

Appendices

Appendix A Femtosecond-four-wave mixing setup
The block diagram of the femtosecond four-wave-mixing setup can be seen in figure 38 which is the same setup as used by Aumanen et al 2014 in reference [16]. The system of two non-collinear optical parametric amplifiers (NOPAs, Orpheus-N, Light Conversion) and laser (Pharos-10, 600 kHz, Light Conversion) was used to generate two ≈ 40 fs pulsed laser beams with wavelengths of 540 nm and 590 nm and partially overlapping pulses in time adjusted by optical delay lines (Thorlabs). The light path of both pulses included neutral density attenuator and one was also installed along with a beam splitter in the path of combined beam which was focused on the sample by microscope objective (Nikon LU Plan ELWD 100x/0.80). The beam splitter was used to split the beam to a camera which was used to view the reflection of laser spot from sample. The scans were made with piezo-stage (Thorlabs NanoMax 300) which was used to move the sample to focus the beam and do scans/patterning in plane. The FWM-image was collected point-by-point by scanning a roster (usually ≈ 100 nm − 300 nm steps) and resulting four-wave-mixing signal was collected in the opposite direction and filtered from the input beam before the measurement and focused to photon counter module SPCM-AQRH-14, (Excelitas Technologies). The sample itself was in an open ended chamber that was flushed during imaging and doping by N_2 3 l min^{-1}. The intensity during imaging and doping was $\approx 1 \times 10^{11}$ W cm^{-2} and an order of magnitude higher for oxidization.

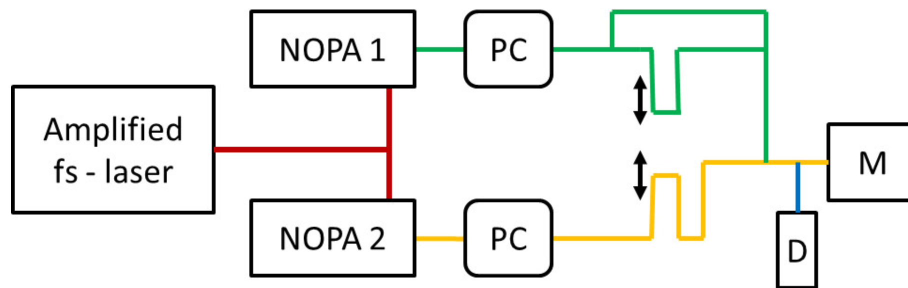

Figure 38. The block-diagram of the femtosecond four-wave-mixing setup which was also used to treat the graphene [57].